A second-order geometry-preserving finite volume method for conservation laws on the sphere

Abdelaziz Beljadid, Philippe G Lefloch, Abdolmajid Mohammadian

A second-order geometry-preserving finite volume method for conservation laws on the sphere

Abdelaziz Beljadid[1,3], Philippe G. LeFloch[2], and Abdolmajid Mohammadian[1]

Abstract

We consider nonlinear hyperbolic conservation laws posed on curved geometries —refered to as "geometric Burgers equations" after Ben-Artzi and LeFloch— when the underlying geometry is the two-dimensional sphere and the flux vector field is determined from a potential function. Despite its apparent simplicity, this hyperbolic model exhibits complex wave phenomena that are not observed in absence of geometrical effects. We formulate a second-order accurate, finite volume method which is based on a latitude/longitude triangulation of the sphere and on a generalized Riemann solver and a direction splitting based on the sphere geometry. Importantly, this scheme is geometry-preserving in the sense that the discrete form of the scheme respects the divergence free condition for the conservation law on the sphere. A total variation diminishing Runge-Kutta method with an operator splitting approach is used for temporal integration. The quality of the numerical solutions is largely improved using the proposed piecewise linear reconstruction and the method performs well for discontinuous solutions with large amplitude and shocks in comparison with the existing schemes. With this method, we numerically investigate the properties of discontinuous solutions and numerically demonstrate the contraction, time-variation monotonicity, and entropy monotonicity properties. Next, we study the late-time asymptotic behavior of solutions, and discuss it in terms of the properties of the flux vector field. We thus provide a rigorous validation of the accuracy and efficiency of the proposed finite volume method in presence of nonlinear hyperbolic waves and a curved geometry. The method should be extendable to the shallow water model posed on the sphere.

1. Introduction

This paper is devoted to nonlinear hyperbolic problems involving conservation laws or, more generally, balance laws and which are posed on curved geometries such as a surface. Our objective is to design robust and efficient numerical approximation methods which allow

[1]Department of Civil Engineering, University of Ottawa, 161 Louis Pasteur, Ottawa, Ontario, K1N6N5, Canada, majid.mohammadian@uottawa.ca

[2]Laboratoire Jacques-Louis Lions & Centre National de la Recherche Scientifique, Université Pierre et Marie Curie (Paris 6), 4 Place Jussieu, 75258 Paris, France. Email: contact@philippelefloch.org

[3]Department of Civil and Environmental Engineering, Massachusetts Institute of Technology, 77 Massachusetts Avenue, Cambridge, Massachusetts 02139, USA, Email: beljadid@mit.edu

to compute discontinuous solutions and preserve the fundamental structure of the partial differential equations, especially geometry-related properties. Hence, our goal is to design and numerically investigate geometry-preserving high-order accurate finite volume methods and to study the late-asymptotic evolution of solutions of hyperbolic systems on the sphere. We advocate the use of a (geometric) formulation of the finite volume method based on the intrinsic (or covariant) form of the equations, rather then the coordinate expression which is more commonly used. In this manner, by properly taking into account the effects induced by the geometry, we can design methods that are, both, accurate and robust.

Compressible fluid dynamics provide a large variety of problems which involve geometrical features. The prototype example is the system of shallow water on the sphere with topography, which describe fluid flows on the surface of the Earth for instance, in connections with weather predictions [20]. Motivated by numerous applications in fluid dynamics, the study of hyperbolic conservation laws posed on curved manifolds were recently initiated in the mathematical and numerical literature. We build here on the work by Ben-Artzi and LeFloch [7] who proposed to rely on an analogue of the inviscid Burgers equation for curved geometry and, more generally, various classes of hyperbolic conservation laws on manifolds. Since Burgers equations has played such an important role in the development of shock-capturing schemes for compressible fluid problems, it is also expected that the class of "geometric Burgers models" should provide an ideal simplified setup in order to design and test geometric-preserving shock-capturing scheme. The mathematical properties of entropy solutions to conservation laws on manifolds (including on spacetimes, that is, with time-dependent (Lorentzian) metrics) were then extensively investigated by LeFloch and co-authors [1, 2, 7, 6] and [25]–[28]. Subsequently, hyperbolic conservation laws on evolving surfaces were studied by Dziuk, Kroöner, and Müller [13] and by Giesselman [15]. More generally, computational methods for evolving surfaces were developped in Dziuk and Elliott [12] and the references therein.

Calhoun et al. (2008) used rectangular quadrilateral and hexahedral grids for solving partial differential equations using circular and spherical domains and grid mappings on the sphere and three-dimensional ball. The authors used the wave-propagation algorithms [31, 24] to discretize hyperbolic systems. Berger et al. (2009) used the quadrilateral grids introduced in Calhoun et al. (2008) to solve shallow water equations (SWEs) on the sphere with adaptive mesh refinement. The authors used the "f-wave" method which was proposed by Bale et al. (2002). The wave-propagation algorithm is defined in this method based on a direct decomposition of flux differences into eigenvectors of approximate Jacobian matrix of the system. LeVeque (2002) provides more discussion about this method.

Giraldo (2001) developed a spectral element method for shallow water system on the sphere. In this method, the generalized icosahedral grid which was introduced by the same author in [14] is used. The SWEs are transformed to Cartesian coordinates using a special mapping and the equations are discretized in conservative form. Giraldo et al. (2002) studied the SWEs on the sphere using Cartesian coordinates augmented with a Lagrange multiplier. The authors developed and evaluated a nodal high-order discontinuous Galerkin method for shallow water system on the sphere. To compute the numerical fluxes, they used the simple Lax-Friedrichs method. In the dissipative term the maximum wave speed

of SWEs which represents the maximum eigenvalue of the Jacobian of the system, is used. Giraldo and Warburton (2005) developed a nodal triangle-based spectral element method for shallow water system on the sphere. Giraldo (2006) developed a triangle-based discontinuous Galerkin method which combines the finite element with finite volume techniques. In its methodology, the author used the Rusanov flux [35] for the numerical fluxes where the viscosity coefficient is chosen locally for each Riemann problem and mentioned that more sophisticated Riemann solvers could be used for the study of the shock wave phenomena. Katta et al.(2015) studied two finite volume methods to solve linear transport problems on the cubed sphere grid system. These numerical methods are based on the central-upwind scheme and high-order reconstructions.

The numerical methods described above are based on solving the classical Riemann problem for hyperbolic systems of conservation laws. The classical Riemann problem for hyperbolic systems is a Cauchy problem with piecewise constant initial data, that is the Cauchy problem with initial condition consisting of two constant states at the left and right of each cell-interface. Note that the resolution is greatly improved when switching from piecewise constant data to piecewise-linear data. This leads to the generalized Riemann problem (GRP), where one-sided function values and their spatial derivatives obtained from high-order reconstructions could be used in the resolution. Ben-Artzi and Falcovitz (2003) provide more details about the resolution of GRP and they show how the solution of GRP could be used as a basic tool in the construction of robust numerical methods. Note that the techniques which are developed to solve the GRP are less employed to design numerical methods. There are many advantages and future interests for the development of numerical schemes using the Generalized Riemann solvers instead of the techniques solving the classical Riemann problem.

We are interested in discontinuous solutions with large amplitude and shocks for hyperbolic systems. Scalar conservation laws will thus be our starting point in the present study and, next, will extend our methodology and conclusions to other hyperbolic equations, such as the shallow water system. To ensure good accuracy of discontinuous solutions with large amplitude and shocks, the numerical methods require the use of sophisticated Riemann solvers. In our case, the Generalized Riemann solvers are used. In the resolution of the GRP, the values of the function and its slopes on the two sides of each cell-interface are used.

The numerical analyses are performed for some aspects which are not understood by analytical methods for discontinuous solutions of hyperbolic systems on the sphere. We numerically investigate the large-time asymptotic behaviors of solutions and some stability properties of the numerical scheme. We thus focus on **geometric Burgers models** and we adopt the methodology proposed in [6] which relies on second–order approximations based on generalized Riemann problems. We propose a scheme which uses a new piecewise linear reconstruction based on the values of the solution at the center of the computational cells and the values of the Riemann solutions at the cell interfaces, using the second-order approximations based on a generalized Riemann solver. In the proposed scheme, we use a total variation diminishing Runge-Kutta method (TVDRK3) with operator splitting for the temporal integration. This **geometric finite volume method** therein is further developed

and numerically investigated. We observe that certain global quantities are conserved by entropy solutions to scalar conservation laws posed on curved geometries. Our aim is therefore to exhibit these global invariants and investigate to which extend they are preserved by (or remain monotone decreasing for) the approximation solutions generated by the geometric method. As has been mentioned before, we are also interested in investigating the large-time asymptotics of solutions which is not understood by analytical method and will be here studied numerically. As we show it in this paper, by distinguishing between several classes of flux vector fields and initial conditions, we can exhibit a variety of nonlinear wave phenomena. Our numerical tests show that the proposed method is consistent with the **maximum principle**, the **entropy stability property** and the **time-variation diminishing property**. The **contraction property** is violated by the scheme and is satisfied only by its first-order version. Our analysis will distinguish between **foliated flux fields** and "generic" (or fully coupled) flux fields. This classification and the character of linearity of the flux are sufficient to predict the late-time asymptotic behavior of the solutions.

An outline of this paper is as follows. In Section 2, we describe the geometric conservation laws and the properties of their entropy solutions. In Section 3 we propose a new classification of flux fields. Section 4 is devoted to classes of solutions of particular interest. In Section 5 we give the description of the geometric finite volume method. Section 6 presents numerical experiments of the spatial and temporal orders of accuracy of the scheme, and numerical tests are performed for nonlinear foliated fluxes, fully coupled flux vector fields, as well as further tests in order to study the asymptotic convergence of solutions. Finally, Section 7 contains concluding remarks.

2. Geometric Burgers models on the sphere

2.1. Geometric hyperbolic conservation laws on manifolds

Fix any compact n-manifold M endowed with a volume form ω with L^∞ regularity. Given a **flux vector field** $F = F(x,u) \in T_xM$ depending on the real parameter u, where x is an arbitrary point on M and T_xM is the tangent space to M at the point x, we consider the **geometric hyperbolic balance law**

$$\partial_t u + \mathrm{div}_\omega F(\cdot,u) = 0 \quad \text{ in } \mathbb{R}_+ \times M, \tag{2.1}$$

with unknown $u : \mathbb{R}_+ \times M \to \mathbb{R}$, where (with some abus of notation) $\mathrm{div}_\omega X = \frac{1}{\omega}\partial_j(\omega X^j)$ with $\omega = \omega dx^1 dx^2 \dots dx^n$ in local coordinates $x = (x^j)_{1\le j\le n}$ and $X = (X^j)$ is an arbitrary vector field, where we use the short-hand notation $\partial_j := \partial/\partial x^j$. We impose that the flux is **geometry-compatible,** in the sense that

$$\mathrm{div}_\omega F(\cdot,\overline{u}) = 0, \tag{2.2}$$

where $\overline{u} \in \mathbb{R}$ is an arbitrary constant which is equivalent to saying that constants are (trivial) solutions of the conservation law. Then, weak solutions are understood in the following sense: for every test-function $\theta = \theta(t,x)$,

$$\iint_{\mathbb{R}_+\times M} \big(\partial_t\theta(t,x)\, u(t,x) + \partial_j\theta(t,x) F^j(x,u(t,x))\big)\, \omega(x) dt dx = 0, \tag{2.3}$$

where F^j denote the components of the vector field F in an arbitrary coordinate chart $x = (x^j)_{1\leq j\leq n}$. Here, we have identified the volume form ω with its expression ωdx in local coordinates (and, for simplicity in order to state (2.3), we have assumed that the manifold is covered by a single chart).

To any equation (2.1) with flux field satisfying the condition (2.2), we can associate a unique **semi–group of entropy solutions** characterized as follows: given any $u_0 \in L^\infty(M)$, there exists a unique entropy solution $u \in L^\infty(\mathbb{R}_+ \times M)$ to the initial value problem

$$\begin{aligned} &\partial_t U(u) + \mathrm{div}_\omega G(\cdot, u) \leq 0, \qquad U'' \geq 0, \\ &u(0) = u_0, \end{aligned} \tag{2.4}$$

in which for every convex function $U : \mathbb{R} \to \mathbb{R}$ we have introduced the corresponding entropy flux $G = G(x, u) \in T_xM$ such that $\partial_u G := U' \partial_u F$. The inequalities in (2.4) are refered to as the **entropy inequalities**.

Moreover, this semi-group of entropy solutions satisfies several fundamental properties:

- **The entropy stability property:** for all $p \in [1, \infty)$ and $t \geq 0$

$$\|u(t)\|_{L^p_\omega(M)} \leq \|u(0)\|_{L^p_\omega(M)}, \tag{2.5}$$

  which also implies the **maximum principle** (by letting $p \to +\infty$):

$$\|u(t)\|_{L^\infty(M)} \leq \|u(0)\|_{L^\infty(M)}, \tag{2.6}$$

  where the p-norm is denoted by $\|.\|_{L^p_\omega(M)}$ which is defined for $p \in [1, \infty)$ and $\|.\|_{L^\infty(M)}$ is the infinity-norm.

- **The L^1 contraction property**: given any two entropy solutions u, v and for all times $t \geq 0$

$$\|v(t) - u(t)\|_{L^1_\omega(M)} \leq \|v(0) - u(0)\|_{L^1_\omega(M)}. \tag{2.7}$$

- **The time-variation diminishing property:** given any entropy solution u

$$\|\partial_t u\|_{\mathcal{M}_\omega(M)}(t) \leq \|\partial_t u\|_{\mathcal{M}_\omega(M)}(0), \qquad t \geq 0, \tag{2.8}$$

  in which $\|\cdot\|_{\mathcal{M}_\omega(M)}$ is the total variation of the corresponding measure (which in the smooth case is nothing but the standard L^1 norm).

We thus have a natural generalization of Kruzkov's theory [22] to a manifold [1, 2, 25, 28]. Geometry-independent bounds hold, which are very useful in designing and testing discrete approximation schemes. The low regularity of the volume form allows us to also include *shock wave in the geometry* (which is relevant to model earthquakes in the context of the shallow water system, for instance).

2.2. The models of interest in this paper

This paper is devoted to the conservation laws on the sphere. We denote by S^2 the unit sphere endowed with a volume form ω and ∇_ω is the covariant derivative operator. We now express the conservation law in the form

$$\partial_t u + \nabla_\omega \cdot (F(\cdot, u)) = 0, \tag{2.9}$$

or equivalently, in local coordinates, we can pose the problem on the unit sphere with a weight function $\omega = \omega(x)$

$$\partial_t u(t,x) + \frac{1}{\omega(x)} \nabla \cdot \big(\omega(x)\, F(x, u(t,x))\big) = 0. \tag{2.10}$$

Flux vector tangent to the sphere can always be expressed in the form

$$F(x,u) = n(x) \wedge \Phi(x,u), \qquad x \in S^2,\, u \in \mathbb{R}, \tag{2.11}$$

where $\Phi = \Phi(x,u)$ is a u-dependent vector field defined in the ambient space $\mathbb{R}^3$, $n = n(x)$ denotes the unit normal vector to the sphere and the symbol $\wedge$ denotes the cross product. As explained earlier, we are primarily interested in geometry-compatible flux vectors satisfying, by definition,

$$\nabla \cdot (F(\cdot, \bar{u})) = 0, \tag{2.12}$$

where $\overline{u}$ is an arbitrary real constant.

Especially, the broad class of **gradient-type flux vector fields** is defined by

$$\Phi(x, \bar{u}) = \nabla h(x, \bar{u}), \qquad x \in S^2, \quad \bar{u} \in \mathbb{R}, \tag{2.13}$$

in which $h = h(x, \bar{u})$ is an arbitrary scalar function and ∇ denotes the gradient operator in $\mathbb{R}^3$. Under these conditions, the flux vector field reads

$$F(x, \bar{u}) = n(x) \wedge \nabla h(x, \bar{u}), \qquad x \in S^2, \quad \bar{u} \in \mathbb{R} \tag{2.14}$$

and we then refer to (2.9) as the **geometric Burgers equations on the sphere** and are determined by a scalar function $h : \mathbb{R}^3 \times \mathbb{R} \to \mathbb{R}$.

We will refer to the function h as the **scalar potential** of the equation. For instance, if h is chosen to be a linear function in the space variable, then Φ is independent of x but its projection on the tangent space of the sphere is still "non-trivial".

3. Classes of flux vector fields

3.1. Foliated flux vector fields

A flux field $F(x,u)$ depends on both the state variable u and the space variable x. For convenience, we adopt the notation $x_j = x^j$ from now on. Roughly speaking, the dependency in x drives the propagation of the waves, while the dependency in u may induce the formation of shocks in the solutions. Some aspects of the influence of the parameters x

and u on the evolution of the solution are observed and analyzed in various cases studied in the numerical tests. To conduct a rigorous numerical analysis, it is useful to introduce some new definitions, which allows us to have the classification of the flux vectors and the type of evolution of solutions. Consider first the dependency in the variable $x \in S^2$. Our analysis has found that the following parameterized level sets $\Gamma_{C,u} = \left\{ x \in \mathbb{R}^3 \,/\, h(x,u) = C \right\}$ play a central role and that the following definition is most relevant.

Definition 3.1. *A gradient flux vector field $F(x,u) = n(x) \wedge \nabla h(x,u)$ defined on the sphere S^2 and associated with a potential function h is called a* **foliated flux field** *if the associated family of level sets $\left\{ \Gamma_{C,u} \right\}_{C \in \mathbb{R}}$ in $\mathbb{R}^3$ is independent of the parameter u, in the sense that for any two u_1, u_2 one can find C_1, C_2 such that $\Gamma_{C_1,u_1} = \Gamma_{C_2,u_2}$.*

As will be confirmed later by our numerical tests, when the foliated condition above holds, the directions of propagation associated with Equation (2.10) depend on the spatial variable x only, and are independent on the variable u; hence, the level sets are determined by the spatial variable only and remain unchanged over time, even under the evolution of the solution. A typical subclass of interest is obtained when h has the following splitting form.

Definition 3.2. *All gradient flux vector field $F(x,u) = n(x) \wedge \nabla h(x,u)$ defined on the sphere S^2 and associated with a potential function h of the form*

$$h(x,u) = \varphi(x) f(u) \tag{3.1}$$

(for an arbitrary φ) are foliated and are referred to as **foliated flux field based on splitting.**

In the latter situation, we obtain decoupled "dynamics" on each level set. If the family of level sets is locally a family of curves, then the conservation laws reduces to a family of one-dimensional equations on each curve.

3.2. Notion of independent domains

When the flux is *not* foliated, we will consider that we are in a "generic" situation and will use the terminology **"generic flux field"** and, in this case, the potential function $h = h(x,u)$ does not have the specific structure exhibited above. Yet, this function can be decomposed into some homogeneous terms and the evolution of the solution is influenced by all those terms, especially, the direction of propagation changes during the evolution, until the solution finally converges asymptotically to some limiting state.

The following notion of "independent domain" on the sphere, presented now, will be of importance in our forthcoming study of the asymptotic convergence of solutions.

Definition 3.3. *Given a gradient flux field, a subset of the sphere S^2 is called an* **independent domain** *if within the family of level sets $\left\{ \Gamma_{C,u} \right\}_{C \in \mathbb{R}}$, one can find one level set that is independent of the parameter u and coincides with the boundary of this domain.*

Such independent domains may exist for foliated flux field as well as generic flux fields. For example, the circle on the sphere defined by $x_1 = 0$ splits the sphere in two independent domains for the foliated flux based on the potential function $h_1(x, u) = x_1 u^2$. The same is true for the generic flux field based on the potential function $h_2(x, u) = x_1 u^2 + x_1 x_2 u^3$.

3.3. Genuine nonlinearity and late-time asymptotics

Consider now the dependency of the scalar potential h in u. A special situation is obtained when the function h is linear in u, and in which case we use the terminology **"linear flux".** The classification that we introduced to distinguish between foliated flux and generic flux, and the character of linearity of the flux are expected to be sufficient to predict the late-time asymptotic behavior of the solutions. The following conjecture is proposed.

Conjecture 3.4. *Under the notation and assumptions* (2.11) *and* (2.13) *and for any initial condition, the following three late-time asymptotic behaviors are expected for entropy solutions of Equation* (2.10)*:*

- *For a linear foliated flux on the entire sphere, the solutions are simply transported within the level sets.*
- *If the flux is foliated with nonlinear behavior on the entire sphere, the solution converges to its constant average in each level set.*
- *The generic flux generates large variations in solutions, which finally converge to constants within independent domains on the sphere.*

In case of fluxes which are linear, foliated or generic only on parts of the sphere, we obtain a combination of the late-time asymptotic behavior of the solutions which depends also on the interaction between the fluxes at boundaries of these parts of the sphere.

This conjecture will be validated numerically in Section 6 using a number of numerical examples.

4. Special classes of solutions

4.1. Wave structure

There are many solutions of particular interest which may have a very rich wave structure, including spatially periodic solutions and steady state solutions. Since for the foliated flux, the system of equations of interest can be reduced to a family of one-dimensional equations on level sets, this type of flux is considered to construct some particular and interesting solutions. The foliated flux with linear behavior is used to obtain the spatially periodic solutions. The foliated flux with nonlinear behavior is employed to construct large families of non-trivial stationary solutions which are used to test the numerical scheme.

4.2. Spherical coordinates

The position of each point on the sphere is specified by its longitude $\lambda \in [0, 2\pi]$ and its latitude $\phi \in [-\pi/2, \pi/2]$. The coordinates are singular at the south and north poles, corresponding to $\phi = -\pi/2$ and $\phi = \pi/2$, respectively. The Cartesian coordinates are denoted by $x = (x_1, x_2, x_3)^T \in \mathbb{R}^3$ with the corresponding standard basis vectors i_1, i_2 and i_3. The spherical coordinates under consideration lead to the following unit normal vector to the sphere.

$$n(x) = \cos\phi\cos\lambda i_1 + \cos\phi\sin\lambda i_2 + \sin\phi i_3,$$

and for each point on the sphere with coordinates (λ, ϕ), we obtain the following unit tangent vectors in the directions of longitude and latitude

$$\begin{aligned} i_\lambda &= -\sin\lambda i_1 + \cos\lambda i_2, \\ i_\phi &= -\sin\phi\cos\lambda i_1 - \sin\phi\sin\lambda i_2 + \cos\phi i_3. \end{aligned}$$

The equation of conservation law (2.10), can be rewritten using the spherical coordinates in the following form:

$$\partial_t u + \frac{1}{\cos\phi}\left(\frac{\partial}{\partial\phi}(F_\phi\cos\phi) + \frac{\partial F_\lambda}{\partial\lambda}\right) = 0, \tag{4.1}$$

where F_λ and F_ϕ are the flux components in spherical coordinates. They are given for each three-dimensional flux of the form $\Phi(x,u) = \tilde{\boldsymbol{f}}_{\boldsymbol{1}}(x,u)i_1 + \tilde{\boldsymbol{f}}_{\boldsymbol{2}}(x,u)i_2 + \tilde{\boldsymbol{f}}_{\boldsymbol{3}}(x,u)i_3$ as follows:

$$\begin{aligned} F(x,u) &= F_\lambda(\lambda,\phi,u)i_\lambda + F_\phi(\lambda,\phi,u)i_\phi, \\ F_\lambda(\lambda,\phi,u) &= \tilde{\boldsymbol{f}}_{\boldsymbol{1}}(x,u)\sin\phi\cos\lambda + \tilde{\boldsymbol{f}}_{\boldsymbol{2}}(x,u)\sin\phi\sin\lambda - \tilde{\boldsymbol{f}}_{\boldsymbol{3}}(x,u)\cos\phi, \\ F_\phi(\lambda,\phi,u) &= -\tilde{\boldsymbol{f}}_{\boldsymbol{1}}(x,u)\sin\lambda + \tilde{\boldsymbol{f}}_{\boldsymbol{2}}(x,u)\cos\lambda. \end{aligned} \tag{4.2}$$

4.3. Solutions for linear foliated flux

We consider the family of linear fluxes defined on the basis of the scalar potential $h(x,u) = \overline{h}(x)u$ with $\overline{h}(x) = -cx_3^d$ for an integer $d \geq 1$ and a real number c chosen arbitrarily. For this case, it is easy to derive the analytical solution for any initial condition $u_0(\lambda,\phi)$

$$\begin{aligned} u(x,t) &= u_0(\lambda - c_\phi t, \phi), \\ c_\phi &= cdx_3^{d-1}. \end{aligned} \tag{4.3}$$

The level sets of this type of fluxes are the circles on the sphere defined by constant latitudes. For $d = 1$ the solution is simply transported within those level sets with the same angular speed and it is globally preserved in a rotating frame. For $d > 1$ the solution is transported within the level sets with different angular speeds and it is preserved in a moving frame along each level set but the solution is not globally preserved. We note that more general forms of the solutions for linear fluxes can be obtained by considering other functions $\overline{h}(x)$.

4.4. Non-trivial steady state solutions

In this section, we present some general classes of non-trivial steady state solutions which will be used in the numerical tests. As mentioned before, foliated fluxes are used to construct non-trivial stationary solutions. More precisely, based on the expected asymptotic behavior for nonlinear foliated flux, the solution of Equation (2.10) evolves along each level set and for a long period of time, this solution converges asymptotically to a constant value on each level set. Thus, it is straightforward (but fundamental) to deduce that for this type of flux, any stationary solution of Equation (2.10) must be constant along each level set. This result is important and further simplifies the problem to find the stationary solutions. However, for the solutions which are used in our numerical tests, it will be proved that they are stationary. In our numerical tests, we will consider the flux vector fields based on the potential function $h(x,u) = \varphi(x)f(u)$, where f is a function of the state variable u and φ is a scalar function defined in $\mathbb{R}^3$. The level sets are the intersections of the sphere with the sets defined as $\varphi(x) = c$, where c are arbitrary constants. The following Corollary describes for the above-mentioned type of flux, a family of non-trivial steady state solutions

Corollary 4.1. ***(A family of steady state solutions).*** *Consider the foliated flux vector $F(x,u) = n(x) \wedge \Phi(x,u)$ with $\Phi = \nabla h$ and $h(x,u) = \varphi(x)f(u)$, where f is a function of the state variable u and φ is a scalar function of class C^1 defined in $\mathbb{R}^3$. For any function $\tilde{u}$ which depends on one variable, the function defined as $u_0(x) = \tilde{u}(\varphi(x))$is a stationary solution to the conservation law* (2.10) *associated to the flux $F(x,u)$.*

This result can be proved using the claim 3.2 in [6]. Since we are interested in discontinuous solutions, the results of Corollary 4.1 will be used to construct discontinuous stationary solutions for some selected flux vectors. In particular, if the same assumptions of the Corollary 4.1 are considered with $f(u) = u^2/2$, then for any function $\tilde{u}$ which depends on one variable, the function defined as $u_0(x) = \chi(\varphi(x))\tilde{u}(\varphi(x))$ is a stationary solution to the conservation law (2.10), where the discrete function χ takes the values ± 1. We will be particularly interested to a linear splitting flux vector defined on the basis of the scalar potential $h(x,u) = (x.a)f(u)$, where as already mentioned $x.a$ denotes the scalar product of the vector x and some constant vector $a \in \mathbb{R}^3$.

5. Geometric finite volume method on the sphere

5.1. Discrete form of the divergence operator

Following [6], we design a Godunov-type, finite volume scheme that is based on an intrinsic approach and provides an accurate treatment of the geometry. Second-order accuracy is obtained with the technique developed by Ben–Artzi and Facolvitz [5], LeFloch and Raviart [29], and Bourgeade et al. [10]. Earlier work was done by Berger et al. [9], Giraldo and collaborators [16, 17, 18, 19], and Rossmanith and collaborators [33, 34] based on high resolution schemes and approximate Riemann solvers by embedding the sphere in a "cubic mesh" in $\mathbb{R}^3$. It should be noted that the computational grid used in this paper is more suitable to apply the proposed techniques. In the following, we present the discrete form

of the geometry-compatible finite volume scheme which was formulated in [6]. In order to ensure a suitable discrete form, an important condition obtained from the theory established by Ben-Artzi and LeFloch [7] called the "zero-divergence" was used in the construction of the scheme.

The grid used in the numerical scheme is shown in Figure 1. Three types of computational cells are used to discretize the sphere. In large area of the sphere, rectangular computational cells are considered. When we go from the equator to the north or south poles, for some special latitude circles, the number of computational cells is reduced by a ratio of 2 by changing the equatorial longitude step in order to respect the condition of stability and to have a homogeneous precision in the entire domain of the sphere. In the intermediate part of the sphere where the equatorial longitude step is changed, computational cells with five sides are used as shown in Figure 1. For this type of computational cells, two sides are collinear. The triangular computational cells are used near the north and south poles which are a special case of the standard rectangular cells with zero length for one side. For the three cases of computational cells, each cell is defined as $\Omega := \{(\lambda, \phi), \lambda_1 \leqslant \lambda \leqslant \lambda_2, \phi_1 \leqslant \phi \leqslant \phi_2\}$. The divergence operator is discretized using the geometry compatibility condition and the flux is approximated using the following formula:

$$(\nabla \cdot (F(x, u(t, x))))^{approx} = \frac{I_i}{\omega_i}, \tag{5.1}$$

where $I_i = (\oint_{\partial\Omega} F(x, u).\nu(x)ds)^{approx}$ which is obtained using the divergence theorem, $\nu(x)$ is the unit normal vector to the boundary $\partial\Omega$ of the cell, ds is the arc length along $\partial\Omega$, and ω_i is the area of the cell. The parameter I_i is calculated for each side e of the cell in terms of the scalar potential h using the following expression:

$$\begin{aligned}
&\Big(\oint_{e_1}^{e_2} F(x, u).\nu(x)ds \Big)^{approx} = \oint_{e_1}^{e_2} (n(x) \wedge \Phi(x, u)).\nu(x)ds \\
&= - \oint_{e_1}^{e_2} \Phi(x, u).(n(x) \wedge \nu(x))ds \\
&= - \oint_{e_1}^{e_2} \nabla h(x, u).\tau(x)ds = - \oint_{e_1}^{e_2} \nabla_{\partial\Omega} h(x, u)ds \\
&= -(h(e_2, u_{12}^m) - h(e_1, u_{12}^m)),
\end{aligned} \tag{5.2}$$

where e_1 and e_2 are, respectively, the initial and final endpoints of the edge e, $\tau(x)$ is the unit tangent vector to the boundary $\partial\Omega$, u_{12}^m is the solution of the Riemann problem in the orthogonal direction to the interface e, and the operator $\nabla_{\partial\Omega}$ is the derivative along the boundary $\partial\Omega$.

It should be noted that the computational grid shown in Figure 1 has a structure which is favorable in order to apply the standard *splitting approach*, as will be described in the section below. We can then solve the generalized Riemann problem at each interface of discontinuity by using the variables λ and ϕ separately. This grid structure also provides a discrete form of the scheme which *exactly satisfies* the "null-divergence" condition.

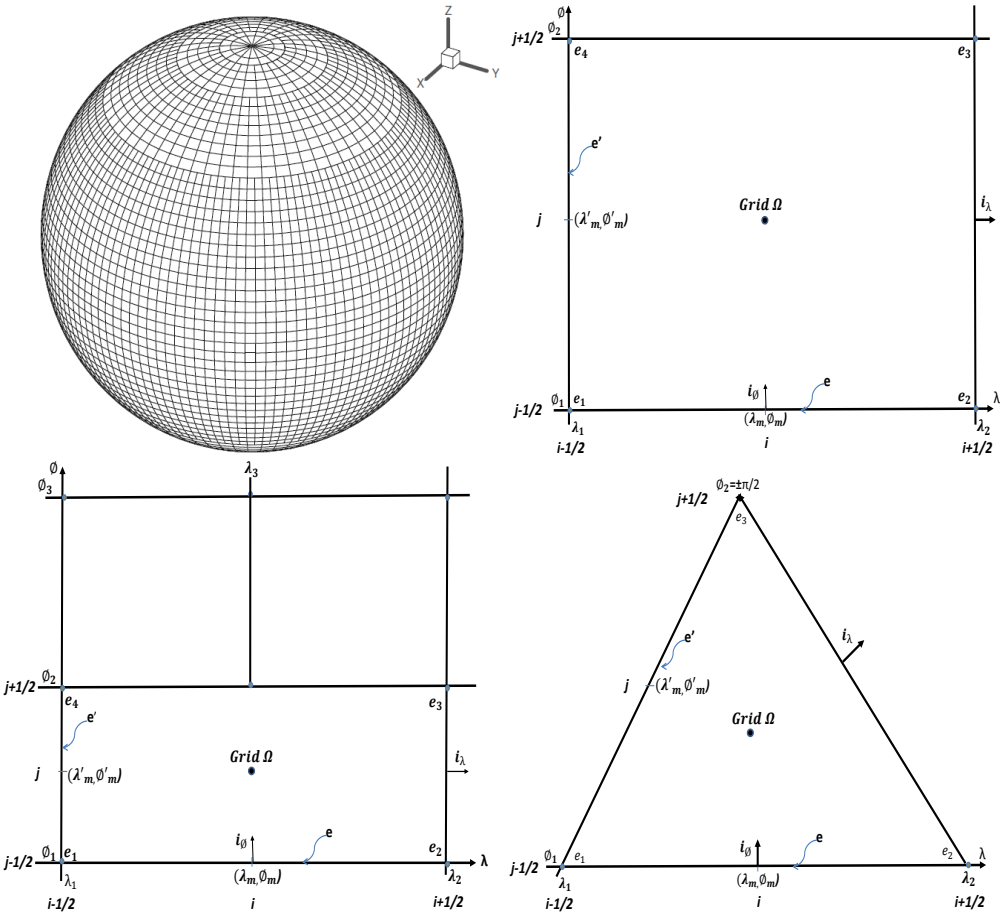

Figure 1: Types of grids used on the sphere

5.2. Equations for the splitting approach

The different approximations used in the numerical scheme are based on the splitting of the equations. Without loss of generality, the following scalar potentials are used to explain the procedure and the different equations of the splitting approach. We used three splitted fluxes which is sufficient to have the possibility to split between the spatial variables x_1, x_2 and x_3.

$$h(x,u) = h_1(x)f_1(u) + h_2(x)f_2(u) + h_3(x)f_3(u), \tag{5.3}$$

which leads to the corresponding gradient flux vector:

$$\begin{aligned}\Phi(x,u) &= \nabla h(x,u)\\ &= \sum_{j=1}^{3} \frac{\partial h_j(x)}{\partial x_1} f_j(u) i_1 + \sum_{j=1}^{3} \frac{\partial h_j(x)}{\partial x_2} f_j(u) i_2 + \sum_{j=1}^{3} \frac{\partial h_j(x)}{\partial x_3} f_j(u) i_3.\end{aligned} \tag{5.4}$$

Using Claim 2.2 in [6], the above expression of $\Phi(x,u)$ as a gradient ensures the validity of the geometry compatibility condition. Equations (4.2) are used to obtain the following flux

components in spherical coordinates:

$$\begin{aligned} F_\lambda(\lambda,\phi,u) &= \Phi_1(x,u)\sin\phi\cos\lambda + \Phi_2(x,u)\sin\phi\sin\lambda - \Phi_3(x,u)\cos\phi, \\ F_\phi(\lambda,\phi,u) &= -\Phi_1(x,u)\sin\lambda + \Phi_2(x,u)\cos\lambda, \end{aligned} \tag{5.5}$$

where $\Phi_i(x,u) = \sum_{j=1}^{3} \frac{\partial h_j(x)}{\partial x_i} f_j(u), i = 1,2,3.$

The geometry compatibility condition is equivalent to the following relation in spherical coordinates which is valid for any constant value $\bar{u} \in \mathbb{R}$:

$$\frac{\partial(F_\phi(\lambda,\phi,\bar{u})\cos\phi)}{\partial\phi} + \frac{\partial F_\lambda(\lambda,\phi,\bar{u})}{\partial\lambda} = 0. \tag{5.6}$$

From (5.5) and (5.6) we derive

$$\begin{aligned} &-\sin\lambda\sum_{j=1}^{3}\frac{\partial h'_{j1}(x)\cos\phi}{\partial\phi}f_j(\bar{u}) + \cos\lambda\sum_{j=1}^{3}\frac{\partial h'_{j2}(x)\ cos\phi}{\partial\phi}f_j(\bar{u}) \\ &+\sin\phi\sum_{j=1}^{3}\frac{\partial h'_{j1}(x)\cos\lambda}{\partial\lambda}f_j(\bar{u}) \\ &+\sin\phi\sum_{j=1}^{3}\frac{\partial h'_{j2}(x)\sin\lambda}{\partial\lambda}f_j(\bar{u}) - \cos\phi\sum_{j=1}^{3}\frac{\partial h'_{j3}(x)}{\partial\lambda}f_j(\bar{u}) = 0, \end{aligned} \tag{5.7}$$

where $h'_{ji}(x) = \frac{\partial h_j(x)}{\partial x_i}$, $i = 1,2,3$ $j = 1,2,3$. Using the conservation law in spherical coordinates (4.1), the flux components given by Equations (5.5), and the geometry-compatibility property formulated by Equation (5.7), one obtains the following equivalent formulation of the conservation law, which is easier to work with:

$$\begin{aligned} &\frac{\partial u}{\partial t} - \sum_{j=1}^{3} h'_{j1}(x)\frac{\partial f_j(u)}{\partial\phi}\sin\lambda + \sum_{j=1}^{3} h'_{j2}(x)\frac{\partial f_j(u)}{\partial\phi}\cos\lambda \\ &+\tan\phi\Big(\sum_{j=1}^{3} h'_{j1}(x)\frac{\partial f_j(u)}{\partial\lambda}\cos\lambda + \sum_{j=1}^{3} h'_{j2}(x)\frac{\partial f_j(u)}{\partial\lambda}\sin\lambda\Big) \\ &-\sum_{j=1}^{3} h'_{j3}(x)\frac{\partial f_j(u)}{\partial\lambda} = 0. \end{aligned} \tag{5.8}$$

Equation (5.8) can be rewritten in the form of balance law which includes a source term. The resulting equation and the splitting approach are used to obtain the Generalized

Riemann Problem values at cell interfaces. We obtain the following "λ split" equations:

$$\begin{aligned}
&\frac{\partial u}{\partial t} + \frac{\partial g(x,u)}{\partial \lambda} = S_\lambda,\\
&g(x,u) = \tan\phi_m \left[\sum_{j=1}^{3} h'_{j1}(x) f_j(u)\cos\lambda + \sum_{j=1}^{3} h'_{j2}(x) f_j(u)\sin\lambda\right]\\
&\qquad\qquad - \sum_{j=1}^{3} h'_{j3}(x) f_j(u),\\
&S_\lambda = \tan\phi_m \left[\sum_{j=1}^{3} f_j(u)\frac{\partial h'_{j1}(x)\cos\lambda}{\partial\lambda} + \sum_{j=1}^{3} f_j(u)\frac{\partial h'_{j2}(x)\sin\lambda}{\partial\lambda}\right]\\
&\qquad - \sum_{j=1}^{3} f_j(u)\frac{\partial h'_{j3}(x)}{\partial\lambda},
\end{aligned} \tag{5.9}$$

where the latitude of the midpoint denoted by ϕ_m is used at each cell interface for the function g. In the following, the notation λ_m is used for the longitude of the midpoint of each cell interface.

For the "ϕ split" equations, one obtains

$$\begin{aligned}
&\frac{\partial u}{\partial t} + \frac{\partial \kappa(x,u)}{\partial \phi} = S_\phi,\\
&\kappa(x,u) = -\sum_{j=1}^{3} h'_{j1}(x) f_j(u)\sin\lambda + \sum_{j=1}^{3} h'_{j2}(x) f_j(u)\cos\lambda,\\
&S_\phi = -\sum_{j=1}^{3} f_j(u)\sin\lambda\frac{\partial h'_{j1}(x)}{\partial\phi} + \sum_{j=1}^{3} f_j(u)\cos\lambda\frac{\partial h'_{j2}(x)}{\partial\phi}.
\end{aligned} \tag{5.10}$$

The right-hand side terms S_λ and S_ϕ of the previous equations are the result of the explicit differentiation of the flux functions $g(x,u)$ and $\kappa(x,u)$. Equations (5.9) and (5.10) are used to obtain the Generalized Riemann Problem values at cell interfaces as explained in the following section.

5.3. Second-order approximations based on generalized Riemann problems

We now present the algorithm used to solve the Generalized Riemann Problem at each cell interface. Since the same method is applied for the equations (5.9) and (5.10), we present the procedure for the case of the "λ split" equations. In the second-order method based on the Generalized Riemann Problem, it is assumed that for any time step t_n, the solution is approximated by a piecewise linear function.

Subject to the initial data for u, the proposed linear reconstruction is used as explained in detail in the next section to obtain the boundary values of u denoted by u_L and u_R and its λ-slopes denoted by $u_{L,\lambda}$ and $u_{R,\lambda}$ at each cell interface of midpoint of coordinates (λ_m, ϕ_m).

The boundary values are used to obtain the solution $\tilde{u}^m$ of the Riemann problem. The Generalized Riemann Problem method uses a linear temporal approximation to obtain the value of the solution of Riemann problem u^m at time $t_n + \Delta t/2$. The approximation of this solution is obtained as:

$$u^m = \tilde{u}^m + \frac{\partial u}{\partial t}(\lambda_m, \phi_m, t_n)\frac{\Delta t}{2}. \tag{5.11}$$

In Equation (5.11), the derivative term is obtained by using the value of the slope of u in the longitude direction at the cell interface which is denoted by $u_{m,\lambda}$

$$\frac{\partial u}{\partial t}(\lambda_m, \phi_m, t_n) = -u_{m,\lambda}\frac{\partial g(x,u)}{\partial u} \mid_{(\lambda_m, \phi_m, \tilde{u}^m)} . \tag{5.12}$$

The parameter $u_{m,\lambda}$ is obtained by the associated Riemann problem. In the following we recall briefly the procedure used to solve the Riemann problem to obtain the values of $\tilde{u}^m$ and the slope $u_{m,\lambda}$.

For $u_L \leq u_R$, we consider the "convex envelope" of g and the solution $\tilde{u}^m$ is obtained as follows:

$$\tilde{u}^m = arg_{v\in[u_L,u_R]} \min(g(x,v) \mid (\lambda_m, \phi_m)). \tag{5.13}$$

There are three cases for this solution and for the slope $u_{m,\lambda}$:

(i) A wave moving to the right:

$$\tilde{u}^m = u_L, \qquad u_{m,\lambda} = u_{L,\lambda}. \tag{5.14}$$

(ii) A wave moving to the left:

$$\tilde{u}^m = u_R, \qquad u_{m,\lambda} = u_{R,\lambda}. \tag{5.15}$$

(iii) A sonic point:

$$u_L < \tilde{u}^m < u_R, \qquad \partial_u g(x,u) \mid_{(\lambda_m, \phi_m, \tilde{u}^m)} = 0. \tag{5.16}$$

Note that for the sonic case, it is easy to conclude, using the equations (5.12) and (5.16), that the time-derivative of u reduces to $\frac{\partial u}{\partial t}(\lambda_m, \phi_m, t_n) = 0$. The geometry-compatibility condition remains valid also for the second-order scheme. Indeed, if we consider the condition $u \equiv const$ in the computational cell and its neighbors, the slopes and the time-derivatives of the generalized Riemann solution vanish and the solution remains constant. Under the condition $u_L > u_R$, the same procedure is used by considering the "concave envelope" of g and the value $\tilde{u}^m$ that maximizes the function $g(x,v)$ with $v \in [u_R, u_L]$. Finally, the same procedure is used for the case of the "ϕ split" equations using the boundary values of u and its ϕ-slopes $u_{L,\phi}$ and $u_{R,\phi}$ at each cell interface.

The same algorithm used for the first step of TVDRK3 method to solve the Generalized Riemann Problem is used for the second and third steps of the method. In the case of the second step of the method, the data $u^{(1)}$ which is obtained from the first step is used instead of the date u. The data $u^{(2)}$ which is obtained from the second step is used to solve the Generalized Riemann Problem in the case of the third step of TVDRK3 method.

5.4. The proposed piecewise linear reconstruction

In this section, we describe the proposed piecewise linear reconstruction in the case of rectangular computational cells where we do not have change of the structure of meshes. The indices i and j are used along the longitude and latitude respectively to locate the position of the centers of computational cells. At each time level t_n, data cell average value $u^n_{i,j}$ in each cell (i,j) of center (λ_i, ϕ_j) is locally replaced by a piecewise linear function. The notation $u^n_{i-1,j}$ and $u^n_{i+1,j}$ are used for the values of the function u at the neighboring cells at the left and right of the cell (i,j). These notations are used with obvious periodicity along the longitude for $i = 1$ and $i = N$, where N is the number of computational cells having the same latitude ϕ_j as the computational cell (i,j). In the case where the mesh structure changes, we consider the same method of reconstruction where we consider the average of the values at the two neighboring cells. For example, at places where there are more cells for latitude ϕ_{j+1} than for ϕ_j, the value $u^n_{i,j+1}$ which will be used in equation (5.20) is the average of the values at the two neighboring cells at latitude ϕ_{j+1}.

The proposed reconstruction leads to the following local function:

$$u^n_{i,j}(\lambda,\phi) = u^n_{i,j} + (\lambda - \lambda_i)\alpha^n_{i,j} + (\phi - \phi_j)\beta^n_{i,j}, \tag{5.17}$$

where $\alpha^n_{i,j}$ and $\beta^n_{i,j}$ are the slopes in the directions of longitude and latitude, respectively. We consider the notation $u^{n\pm}_{i+\frac{1}{2},j}$ for the corresponding right and left values of u at the interface $(i+\frac{1}{2}, j)$ in the longitude direction which are obtained by using the proposed piecewise linear reconstruction at time t_n. In the same way the notation $u^{n\pm}_{i,j+\frac{1}{2}}$ is used for the right and left values at the interface $(i, j+\frac{1}{2})$ in the latitude direction for the function u at time t_n. These values are used to obtain the associated Riemann values which are denoted by $u^n_{i+\frac{1}{2},j}$ and $u^n_{i,j+\frac{1}{2}}$ at the interfaces $(i+\frac{1}{2}, j)$ and $(i, j+\frac{1}{2})$, respectively.

The slope $\alpha^n_{i,j}$ is obtained by using the following steps:

$$\begin{aligned}
\tilde{u}^n_{i+\frac{1}{2},j} &= u^{n-1}_{i+\frac{1}{2},j} + (\frac{\partial u}{\partial t})^{n-1}_{i+\frac{1}{2},j}(t_n - t_{n-1}),\\
\tilde{\alpha}^n_{i,j} &= \frac{1}{\Delta\lambda}(\tilde{u}^n_{i+\frac{1}{2},j} - \tilde{u}^n_{i-\frac{1}{2},j}),\\
\alpha^n_{i,j} &= \frac{1}{\Delta\lambda}\ minmod((u^n_{i+1,j} - u^n_{i,j})), \Delta\lambda\tilde{\alpha}^n_{i,j}, (u^n_{i,j} - u^n_{i-1,j})),
\end{aligned} \tag{5.18}$$

where $u^{n-1}_{i+\frac{1}{2},j}$ is the solution of the Riemann problem at the interface $(i+\frac{1}{2}, j)$ which is obtained in the previous step t_{n-1} using the procedure explained in Section 5.3. The value of $\tilde{u}^n_{i+\frac{1}{2},j}$ computed using the first equation in (5.18) based on the data from step t_{n-1} is an approximation of the solution of the Riemann problem at the interface $(i+\frac{1}{2}, j)$ at time t_n . The time-derivative $(\frac{\partial u}{\partial t})^{n-1}_{i+\frac{1}{2},j}$ in (5.18) is computed in the previous step t_{n-1} using Equation (5.12). In the third equation of (5.18) we use the multivariable minmod function defined as

$$\begin{aligned}
&minmod(\sigma_1, \sigma_2, \sigma_3)\\
&= \begin{cases} \sigma \min(|\sigma_1|, |\sigma_2|, |\sigma_3|), & if\ sign(\sigma_1) = sign(\sigma_2) = sign(\sigma_3) = \sigma,\\ 0. & \text{otherwise.} \end{cases}
\end{aligned} \tag{5.19}$$

In the same way the slope $\beta^n_{i,j}$ is obtained by using the following steps:

$$\begin{aligned}
\tilde{u}^n_{i,j+\frac{1}{2}} &= u^{n-1}_{i,j+\frac{1}{2}} + (\frac{\partial u}{\partial t})^{n-1}_{i,j+\frac{1}{2}}(t_n - t_{n-1}),\\
\tilde{\beta}^n_{i,j} &= \frac{1}{\Delta\phi}(\tilde{u}^n_{i,j+\frac{1}{2}} - \tilde{u}^n_{i,j-\frac{1}{2}}),\\
\beta^n_{i,j} &= \frac{1}{\Delta\phi}\ minmod((u^n_{i,j+1} - u^n_{i,j})), \Delta\phi\tilde{\beta}^n_{i,j}, (u^n_{i,j} - u^n_{i,j-1})),
\end{aligned} \tag{5.20}$$

where $u^{n-1}_{i,j+\frac{1}{2}}$ is the solution in the previous step t_{n-1} of the Riemann problem at the cell interface $(i, j+\frac{1}{2})$ which is obtained by using the same procedure explained in Section 5.3 for the case of the "ϕ split" equations. The value of $\tilde{u}^n_{i,j+\frac{1}{2}}$ is obtained by using the first equation in (5.20). This value is an approximation of the solution of the Riemann problem at the interface $(i, j+\frac{1}{2})$ at time t_n. The value of the time-derivative $(\frac{\partial u}{\partial t})^{n-1}_{i,j+\frac{1}{2}}$ is obtained in the previous step t_{n-1} using an equation similar to (5.12), and by using the slope $u_{m,\phi}$ of u in the latitude direction at the cell interface.

5.5. Description of the scheme

In this section, we summarize the steps used in the finite volume method. At each time level t_n, data cell average values $u^n_{i,j}$ are used to obtain the linear reconstruction based on the slopes computed using equations (5.18) and (5.20). It should be mentioned that for the first step of the scheme we do not have any data of the state variable u from any previous step. In order to start the method, for the proposed piecewise linear reconstruction, the third equations in (5.18) and (5.20) are used to obtain the slopes $\alpha^n_{i,j}$ and $\beta^n_{i,j}$, respectively, without using the parameters $\tilde{\alpha}^n_{i,j}$ and $\tilde{\beta}^n_{i,j}$. For this case, the data cell average values $u^n_{i,j}$ are used with a two-variable minmod function. In general at each time level t_n, equations (5.18) and (5.20) are used to obtain the slopes $\alpha^n_{i,j}$ and $\beta^n_{i,j}$, respectively, using the data of u at time level t_n and the solution of the Generalized Riemann Problem at the previous time step t_{n-1}.

For the first step of TVDRK3 method, the obtained linear reconstruction from the data cell average values $u^n_{i,j}$ are used to obtain the boundary values u_L and u_R, and the slopes $u_{L,\lambda}$ and $u_{R,\lambda}$ at each cell interface. The generalized Riemann values at the cell interfaces at time level t_n are obtained using Equation (5.11) as already explained in Section 5.4.

The splitting approach is used and Equations (5.9) and (5.10) are solved to obtain the values $u^{(1)}_{i,j}$ in the first step TVDRK3 method. For the second step of TVDRK3 method, the data cell average values $u^{(1)}_{i,j}$ are used to obtain the linear reconstruction, the boundary values and the generalized Riemann values at the cell interfaces using Equation (5.11). Equations (5.9) and (5.10) are solved to obtain the values $u^{(2)}_{i,j}$. The same procedure is used for the third step of TVDRK3 method. The data cell average values $u^{(2)}_{i,j}$ are used to obtain the linear reconstruction, the boundary values, the generalized Riemann values at the cell interfaces and the cell average values $u^{n+1}_{i,j}$ of the state variable at the next step t_{n+1}.

6. Numerical experiments

6.1. Numerical analysis of the spatial and temporal orders of accuracy of the scheme

6.1.1. Spatial order of the scheme

Two numerical tests are performed in order to determine experimentally the spatial order of accuracy of the proposed scheme. We used the nonlinear foliated flux defined from the scalar potential $h(x,u) = (x.a)f(u)$ with $f(u) = u^2/2$. In the first test, we consider the flux with $a = i_1$ and, as initial data, the three (steady state) functions: $u_1(0,x) = x_1$, $u_2(0,x) = x_1\cosh(x_1)$, and $u_3(0,x) = x_1^3\sin x_1$. For the second test, we use the flux with $a = i_1+i_2+i_3$ and, as initial data, the three steady state solutions: $v_1(0,x) = \sinh\theta/(1+\theta^2)$, $v_2(0,x) = (1-\theta)e^{\theta}$, and $v_3(0,x) = \theta^3$ with $\theta = x_1 + x_2 + x_3$.

To determine numerically the spatial convergence rate, we use a very small time step $\Delta t = 0.0001$ in order to render the temporal errors negligible. Different sizes of the computational cells are used to obtain the evolution of the error. We use the longitude step $\Delta\lambda$ and the latitude step $\Delta\phi$ with the same order, and to evaluate the errors, we use the mesh-size weighted L^1-norm. Figure 2 shows the evolution of the L^1-error in a log-log scale up to the time $T = 5$ for the first and second tests. For both choices of flux and for all the initial conditions under consideration, we observe that for small sizes of the computational cells the spatial convergence rate is approximately equal to 2. This result confirms the second-order of spatial accuracy of the scheme studied in this paper.

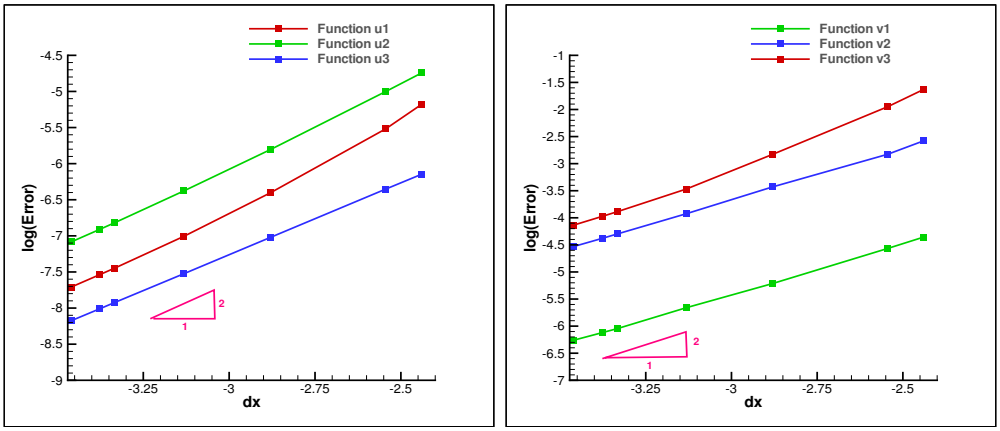

Figure 2: Evolution of L^1-error in log-log scale until time $T = 5$ ($dx = \log(\Delta\lambda)$) for the nonlinear foliated flux defined on the basis of the scalar potential $h(x,u) = (x.a)f(u)$. Left: For the nonlinear foliated flux defined by using $a = i_1$. Right: For the nonlinear foliated flux defined by using $a = i_1 + i_2 + i_3$.

6.1.2. Impact of the splitting approach on the temporal order of the scheme

In this section, we study the impact of the splitting approach on the third-order of the TVD Runge-Kutta method used for time integration in the scheme. The experimental determination of the temporal accuracy is more challenging since the combined effects of spatial and temporal errors are, in general, difficult to distinguish. The use of a very small size of the computational cells to reduce the spatial errors is not possible since the stability

condition limiting the ratio value $\vartheta\Delta t/L_{cell}$ should be satisfied for each cell, where L_{cell} is the minimum distance inside the cell from its center, and ϑ is the wave speed. We will use the algorithm used by Bona et al. [8] to numerically obtain the order of temporal accuracy of the proposed method.

For a fixed size of mesh $\Delta\lambda = \Delta\phi$, we consider a reference solution at time T denoted by u_{ref} which is obtained by using a very small time step Δt_{ref}. This reference solution will differ from the exact solution by an error that is almost purely from the spatial discretization. This solution is used in the numerical tests in order to cancel the spatial errors. For a fixed spatial size $\Delta\lambda$ of the computational cell, a modified error at time T denoted by $\tilde{E}$ is defined using the L^1-norm. This modified error is computed for values of time steps Δt that are larger than Δt_{ref}, using the following formulas:

$$\tilde{E}(T,\Delta t) = \left\| u^{(n)}(\Delta\lambda,\Delta t) - u^{(n)}_{ref}(\Delta\lambda,\Delta t_{ref}) \right\|_{L^1} / \left\| u^{(a)} \right\|_{L^1}, \tag{6.1}$$

where $u^{(a)}$ is the analytical solution and $u^{(n)}$ is the numerical solution obtained by using a time step Δt and the same spatial step $\Delta\lambda$ used for the reference solution $u^{(n)}_{ref}$.

For small values of Δt which are larger than Δt_{ref}, the temporal rate of convergence of the proposed scheme can be visible because when we subtract the reference solution $u^{(n)}_{ref}(\Delta\lambda,\Delta t_{ref})$ from the approximate solution $u^{(n)}(\Delta\lambda,\Delta t)$, the spatial errors are almost canceled. In order to experimentally check the order of accuracy of the proposed temporal scheme which combines the TVDRK3 method with the splitting approach a numerical test is performed using the nonlinear foliated flux defined based on the scalar potential $h(x,u) = (x.a)f(u)$ with $f(u) = u^2/2$ and $a = i_1$. The proposed scheme is applied to the system (4.1) subject to the initial condition (steady state solution) $u(0,x) = x_1^3$.

The temporal rate of convergence at time $T = 5$ is shown in Table 1 for $\Delta t_{ref} = 0.0001$. The results confirm that the splitting method has less impact on the third order accuracy of the TVD Runge-Kutta method used for temporal integration.

Table 1: Temporal rate of convergence of the proposed scheme at $T = 5$.

Δt	1E-03	2E-03	4 E-03	6 E-03	1 E-02
Rate	3.00	3.00	3.00	2.99	2.98

6.2. First test case with linear foliated flux

Referring to Section 4.3, here we perform two tests cases using linear fluxes based on different scalar potentials $h(x,u) = \overline{h}(x)u$. We consider a grid with an equatorial longitude step $\Delta\lambda = \pi/96$ and a latitude step $\Delta\phi = \pi/96$, and a time step $\Delta t = 0.01$. In the first numerical test (Test 1-a), the function $\overline{h}(x) = -x_3$ is considered, which leads to the following flux vector:

$$F_\lambda(\lambda,\phi,\lambda) = \cos\phi u, \qquad F_\phi(\lambda,\phi,\lambda) = 0. \tag{6.2}$$

We consider the initial condition with a discontinuity along the curve $x_1 = 0$, defined as:

$$u(0,x) = \begin{cases} \cos\phi, & x_1 \geq 0, \\ -\cos\phi, & \text{otherwise.} \end{cases} \tag{6.3}$$

For this case, the solution is transported with the same angular speed along the level sets which are the circles defined by $\phi = \phi_c$, where $\phi_c \in [-\pi/2, \pi/2]$. Figure 3, on the left, shows the solution at time $t = 50$ and confirms that it is globally preserved in rotating frame on the sphere.

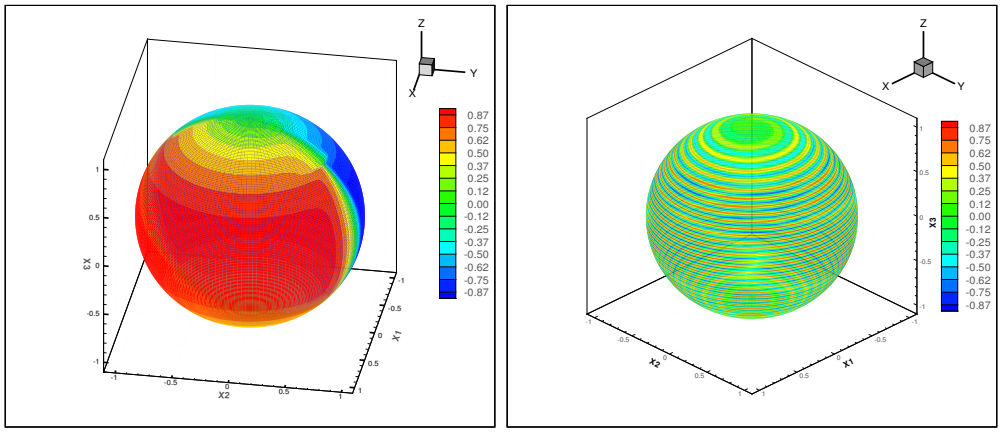

Figure 3: Solutions of Test 1-a (left) and Test 1-b (right) at time $t = 50$ with $\Delta t = 0.01$, $\Delta\lambda = \pi/96$, and $\Delta\phi = \pi/96$.

Now we consider the second test (test 1-b) in which the flux vector is defined on the basis of the scalar potential $h(x,u) = -x_3^2 u$, and the same initial condition is used as in the first test. For this test, again the solution is transported along the same level sets but with different angular speeds. As shown in Figure 3, on the right, the solution is preserved at time $t = 50$ on each level set in a moving frame but not globally preserved on the sphere.

6.3. Second test case with nonlinear foliated fluxes

In this section several aspects will be analyzed for a nonlinear foliated flux of the form $F(x,u) = f(u)n(x) \wedge i_1$ with $f(u) = u^2/2$. The evolution of L^1- error of the proposed scheme is analyzed using discontinuous steady state solutions. The entropy stability property (2.5), the time-variation diminishing property (2.8), and the contraction property (2.7), are analyzed for the first and second order of the scheme. The late-time asymptotic behaviors of the solutions are analyzed using this flux and different initial conditions.

First, we consider the following discontinuous steady state solution of Equation (2.10) which is taken as an initial condition (test 2-a).

$$u_1(0,x) = \begin{cases} 1, & x_1 \leq 0, \\ -1, & \text{otherwise.} \end{cases} \tag{6.4}$$

In this test we compute the numerical solution by using the computational cell with equatorial longitude step $\Delta\lambda = \pi/96$ and latitude step $\Delta\phi = \pi/96$, and a time step $\Delta t = 0.03$.

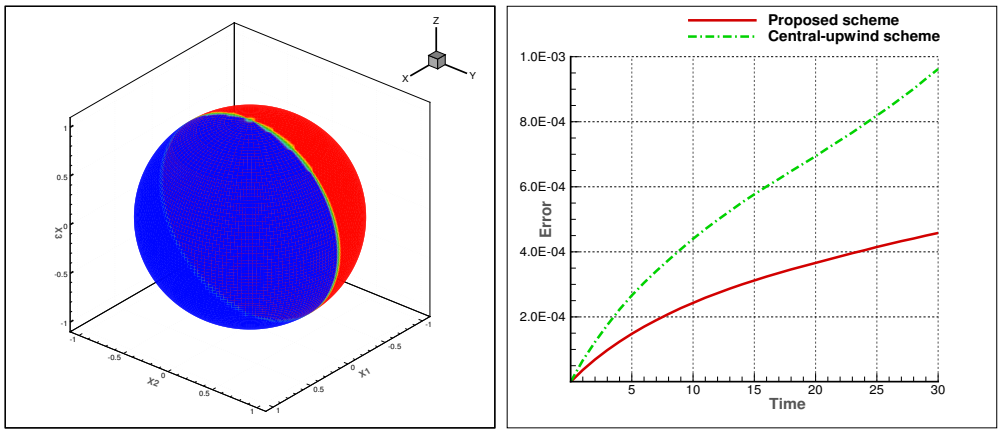

Figure 4: Solution of Test 2-a on the entire sphere (left) at time $t = 100$. Evolution of L^1-error of the solution until time $t = 30$ for Test 2-b (right) using the proposed scheme and Central-upwind scheme with $\gamma = 0.1$. The grid with $\Delta\lambda = \pi/96$ and $\Delta\phi = \pi/96$ is used for the two tests cases.

A two-dimensional view of the solution at time $t = 100$ is presented in Figure 4 (left) which confirms that the solution remains unchanged over the entire sphere. The numerical solution is in good agreement with the initial condition and it remains steady state. Now we consider a new test (Test 2-b) using the following steady state solution, with more discontinuities, which is defined in three domains separated by two closed curves on the sphere defining these discontinuities.

$$u_2(x) = \begin{cases} \gamma x_1^3, & -1 \le x_1 \le -0.5, \\ 0.5\gamma x_1^2, & -0.5 < x_1 < 0.5, \\ -0.25\gamma x_1, & 0.5 \le x_1 \le 1, \end{cases} \tag{6.5}$$

where the parameter γ is introduced in order to control the amplitude and shocks of the solution.

The numerical solution is computed by using the same computational grid as that considered in the previous test and a time step $\Delta t = 0.03$. Figure 4, on the right, shows the evolution of L^1-error of the solution (6.5) with $\gamma = 0.1$ until time $t = 30$ using the proposed scheme and the extension of the central-upwind scheme developed by Kurganov and Petrova in [23] to the spherical case. The proposed scheme performs much better than the central-upwind scheme especially for the discontinuous solutions with large amplitudes and shocks. For $\gamma = 0.3$ at time $t = 5$, we obtain the L^1-error of 9.3×10^{-4} for the proposed method and the error of 1.7×10^{-3} for the central-upwind scheme.

Figure 5 shows the numerical solution on the equator of the sphere at time $t = 5$ using the initial condition (6.5) for the two cases $\gamma = 0.1$ (left) and $\gamma = 0.3$ (right). The numerical solution is in good agreement with the analytical steady-state solution (6.5).

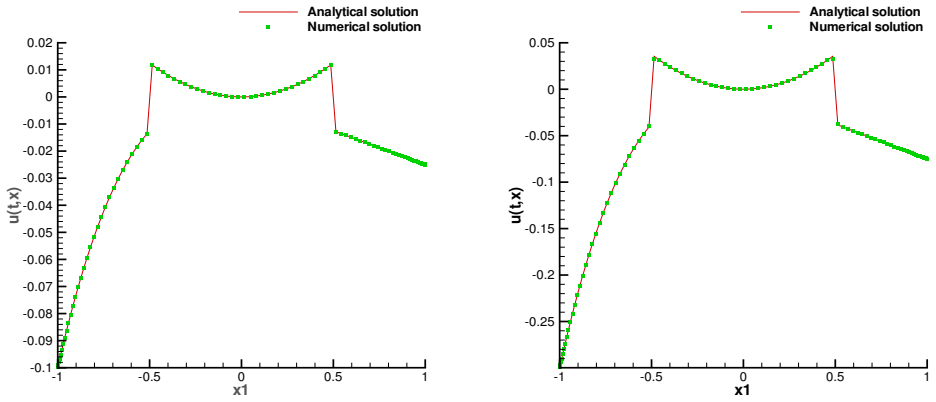

Figure 5: Solutions of Test 2.b at time $t = 5$ for the cases $\gamma = 0.1$ (left) and $\gamma = 0.3$ (right) using the proposed method with $\Delta t = 0.03$, $\Delta\lambda = \pi/96$, and $\Delta\phi = \pi/96$.

According to the scalar potential $h(x, u) = x_1 u^2/2$, the circle defined on the sphere by $x_1 = 0$ splits the sphere into two independent domains, the first domain includes the points with $x_1 \geq 0$ and the second includes the points with $x_1 < 0$. The average values of the initial condition in the first and second domains are denoted by $\overline{u}_I$ and $\overline{u}_{II}$, respectively.

The numerical test for large simulation time is performed using the same computational grid with equatorial longitude step $\Delta\lambda = \pi/96$ and latitude step $\Delta\phi = \pi/96$, and we used a time step $\Delta t = 0.03$. The use of the same grid influences the computed solution and allows us to obtain other types of steady state solutions, where we observe that they are captured by the numerical scheme using this computational grid.

Figure 6, at the left, shows that the parameters $\|u(t) - \overline{u}_I\|_{L^1}$ and $\|u(t) - \overline{u}_{II}\|_{L^1}$ in the first and second domains of the sphere, respectively, are decreasing over time and tend to zero for a large simulation time. The solution converges asymptotically to different constant values in those domains and the convergence is faster in the second domain than the first domain.

Figure 6, on the right, presents the two-dimensional view of the solution for a large simulation time and shows that the solution has almost reached an asymptotic convergence.

Following our numerical experiments, the parameter $\|u(t)\|_{L^p_\omega(M)}$ using L^p norm for $p = 1, 2, 3, 4, 5, 10$ and ∞, is decreasing with time which confirms that the entropy stability property (2.5) is verified for all those norms.

Several tests were performed using the following functions in order to verify the time-variation diminishing property (2.8). As shown in Figure 7, this property holds for both cases of the first and second order of the scheme.

$$u_1(0, x) = \begin{cases} \sin\lambda, & x_1 \geq 0, \\ -\sin\lambda, & \text{otherwise}, \end{cases} \tag{6.6}$$

$$u_2(0, x) = \begin{cases} x_3, & \lambda \leq \pi, \\ x_3 \cos\lambda, & \text{otherwise}, \end{cases} \tag{6.7}$$

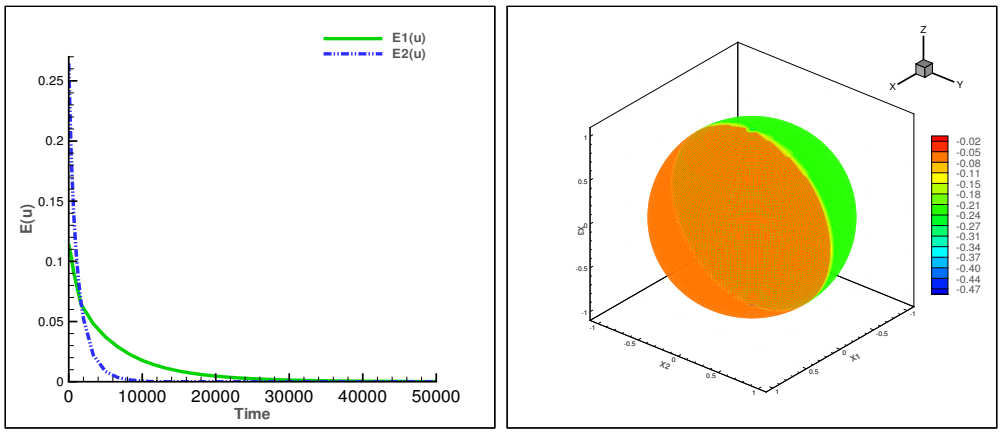

Figure 6: Convergence for Test 2-b using $\gamma = 1$. Left: Evolution of the parameters $E_1(u) = \|u(t) - \overline{u}_I\|_{L^1}$ in domain 1 and $E_2(u) = \|u(t) - \overline{u}_{II}\|_{L^1}$ in domain 2 with $\Delta t = 0.05$, $\Delta\lambda = \pi/96$ and $\Delta\phi = \pi/96$. Right: Two-dimensional view of the solution at time $t = 50000$.

$$u_3(0,x) = \begin{cases} x_2, & x_1 \leq 0, \\ -x_2 e^{x_1}, & \text{otherwise}, \end{cases} \tag{6.8}$$

$$u_4(0,x) = \begin{cases} \frac{1}{\theta - 1}, & \theta < 0, \\ \frac{1}{1+\theta^2}, & 0 \leq \theta \leq 2/\sqrt{3}, \\ -3/7, & \text{otherwise}, \end{cases} \tag{6.9}$$

where $\theta = x_1 + 2x_2 + x_3$.

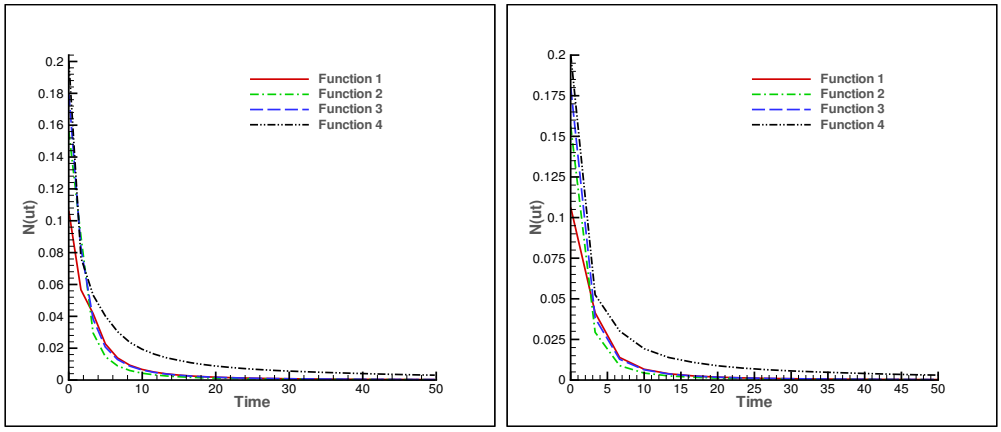

Figure 7: Time-variation diminishing property (2.8) for the first order of the scheme (left) and for the second order of the scheme (right) until time $t = 50$ with $\Delta t = 0.01$, $\Delta\lambda = \pi/96$ and $\Delta\phi = \pi/96$.

We now proceed to the analysis of the contraction property (2.7) for the numerical scheme using the L^1-norm. We start by giving an example of two functions which verify the contraction property for the first-order scheme but they do not verify this property for the

second-order method. We consider the functions v_1 and w_1 defined by:

$$v_1(0,x) = \begin{cases} x_1 + x_3^2, & x_1 > 0, \\ -x_1 - x_3^2, & \text{otherwise}, \end{cases} \qquad (6.10)$$
$$w_1(0,x) = |x_1|.$$

Figure 8, on the left, shows the evolution of the ratio $E(v,w)$ defined by the following formula and confirms that this parameter is decreasing only in the case of the first-order scheme.

$$E(v,w) = \|v(t) - w(t)\|_{L^1_\omega(M)} / \|v(0) - w(0)\|_{L^1_\omega(M)}. \qquad (6.11)$$

Several tests are performed to verify the contraction property (2.7) for the first-order scheme using the five pairs of functions given in Appendix I-1. Figure 8, on the right, shows the evolution of the ratio $E(v,w)$ for the five pairs of functions. This parameter is decreasing for all cases, which confirms that the contraction property (2.7) is valid for all pairs of functions considered.

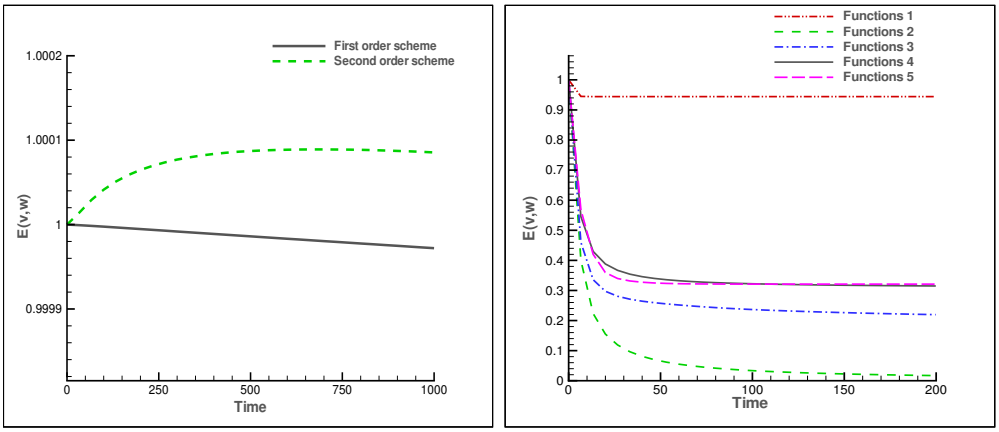

Figure 8: Contraction property (2.7) with $\Delta t = 0.01$, $\Delta\lambda = \pi/96$ and $\Delta\phi = \pi/96$. Left : for the case of the first and second order schemes. Right: for the case of the first-order scheme using several functions.

6.4. Third test case with nonlinear foliated fluxes – alternative forms

We consider the nonlinear foliated flux $F(x,u) = f(u)n(x) \wedge (i_1 + i_2 + i_3)$ which corresponds to the scalar potential $h(x,u) = (x_1 + x_2 + x_3)f(u)$ with $f(u) = u^2/2$. Following the Corollary 4.1, for this flux any function of the form $u_0(x) = \tilde{u}(x_1 + x_2 + x_3)$ is a steady state solution of Equation (2.10), where $\tilde{u}$ is an arbitrary real function depending on one variable. In this section the tests are performed using the following discontinuous steady state solution:

$$u_1(0,x) = \begin{cases} k\frac{\theta^3+1}{5-\theta}, & -\sqrt{3} \le \theta \le 0, \\ k(\theta^2 - \theta - 1/5), & \text{otherwise}, \end{cases} \qquad (6.12)$$

where $\theta = x_1 + x_2 + x_3$ and $\theta \in [-\sqrt{3}, \sqrt{3}]$. The parameter k is used to control the amplitude and shocks of the solution (6.12).

The present test (3-a) is performed with the above function as an initial condition, using a grid with an equatorial longitude step $\Delta\lambda = \pi/96$ and a latitude step $\Delta\phi = \pi/96$, and a time step $\Delta t = 0.02$. Figure 9 (left) shows the evolution of L^1-error of the solution until time $t = 30$ using three cases of values of the parameter k and confirms that the proposed scheme performs well for discontinuous solutions.

The numerical test for large simulation time is performed using the same computational grid which influences the computed solution and allows us to obtain other steady state solutions. Figure 9, on the right, shows the evolution of the parameter $\|u_1(t) - \overline{u}_1\|_{L^1}$ using the solution (6.12) with $k = 1$, where $\overline{u}_1$ is the average value of this solution on the sphere. For a large simulation time, the numerical solution converges to a constant value on the entire sphere.

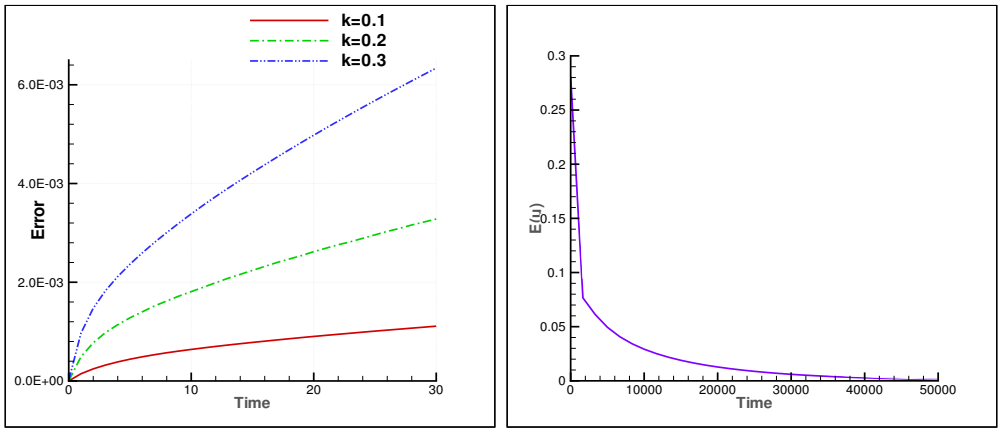

Figure 9: Left: Evolution of L^1-error for Test 3-a until time $t = 30$ with $\Delta t = 0.02$, $\Delta\lambda = \pi/96$ and $\Delta\phi = \pi/96$ for the three cases $k = 0.1$, $k = 0.2$ and $k = 0.3$. Right: Evolution of $\|u_1(t) - \overline{u}_1\|_{L^1}$ for large simulation time with $\Delta t = 0.05$, $\Delta\lambda = \pi/96$ and $\Delta\phi = \pi/96$

The entropy stability property (2.5) is analyzed using the entropy solution (6.12) with the L^p-norm for $p = 1, 2, 3, 4, 5, 10$ and ∞. As shown in Figure 10, this property is checked for all those norms. The time-variation diminishing property (2.8) is now checked for the first and second order schemes using the L^1-norm and the following functions:

$$u_1(0,x) = \begin{cases} x_2 + \theta x_1, & -\sqrt{3} \le \theta \le 0, \\ -x_2 + \theta x_3, & \text{otherwise}, \end{cases}$$

$$u_2(0,x) = \begin{cases} x_1 + x_2\cos\lambda, & 0 \le \lambda \le \pi/2, \\ -x_1, & \pi/2 < \lambda < \pi, \\ x_1 + x_3\sin\lambda, & \text{otherwise}, \end{cases} \tag{6.13}$$

$$u_3(0,x) = \begin{cases} \theta e^{x_3} + e^{\theta}, & -\sqrt{3} \le \theta \le 0, \\ -1 + \theta\log\theta, & \text{otherwise}, \end{cases}$$

$$u_4(0,x) = \begin{cases} x_2\sinh(x_1) + \frac{1}{x_1^2+4}, & -1 \le x_1 \le 0, \\ -\cosh(x_1)/4, & \text{otherwise}. \end{cases} \tag{6.14}$$

Figure 10, on the right, presents the evolution of the parameter $\|\partial_t u\|_{\mathcal{M}}(t)$ for the first-order scheme. Figure 11, on the left, shows the evolution of this parameter for the second-order scheme. This parameter decreases over time, which shows that the time-variation diminishing property (2.8) is valid for all the functions arbitrarily chosen for the first and second order schemes.

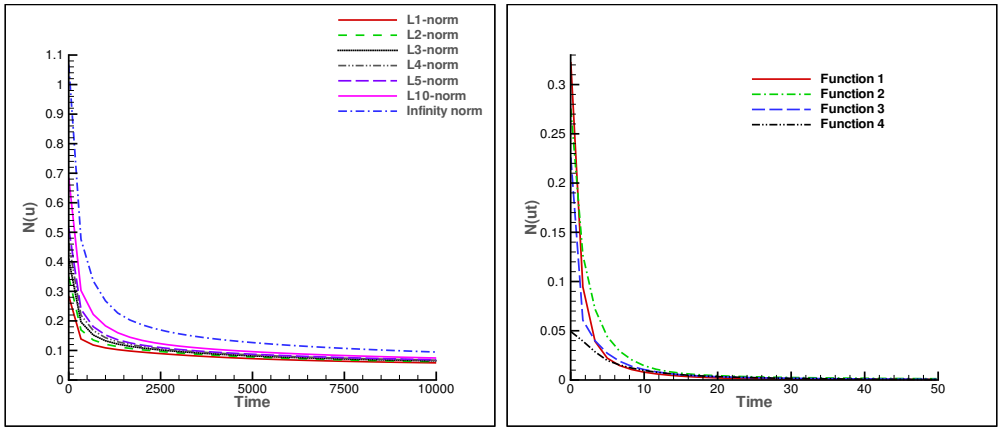

Figure 10: Stability property for Test 3-a (left) and property (2.8) for the first-order scheme until time $t = 50$ (right) with $k = 1$, $\Delta t = 0.01$, $\Delta\lambda = \pi/96$ and $\Delta\phi = \pi/96$.

The contraction property (2.7) is now validated for the first-order scheme using the five pairs of functions given in Appendix I-2. As shown in Figure 11, on the right, the ratios $E(v, w)$ defined by Equation (6.11) are decreasing, which confirms that the contraction property (2.7) is valid for all those pairs of functions.

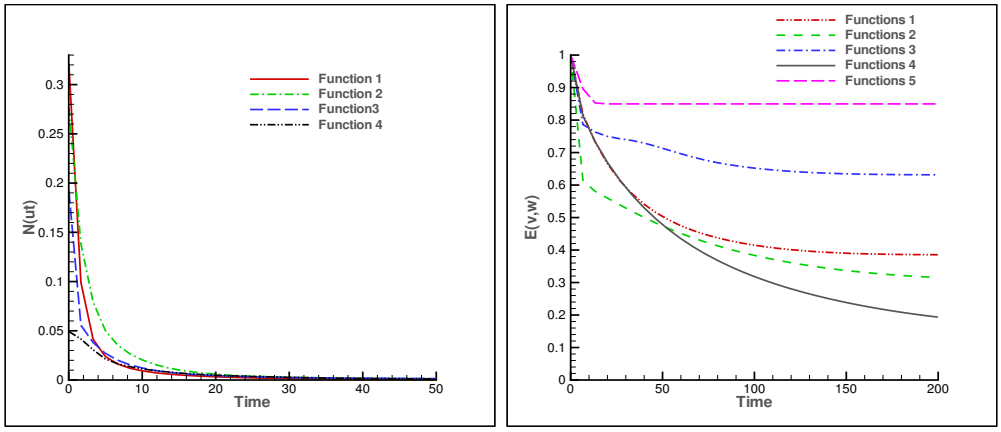

Figure 11: Property (2.8) for the second-order scheme until time $t = 50$ (left) and contraction property (2.7) for the first-order scheme (right) with $\Delta t = 0.01$, $\Delta\lambda = \pi/96$ and $\Delta\phi = \pi/96$.

In the following other non-trivial steady state solutions with more general forms will be considered to test the accuracy of the scheme. We consider the nonlinear foliated flux based on the potential function $h(x, u) = \varphi(x)f(u)$. For this case, the function $u_0(x) = \tilde{u}(\varphi(x))$

is a stationary solution to the conservation law (2.10), where $\tilde{u}$ is a function which depends on one variable. Arbitrary functions φ are selected in order to obtain non-trivial stationary solutions with level sets which have different and more complex forms on the sphere. These steady state solutions are very relevant to test the accuracy of the numerical scheme.

The numerical tests are performed for four cases using the functions $\varphi_1(x) = -x_1^2+x_2+x_3$, $\varphi_2(x) = -x_1^2 + x_2^3 + x_3$, $\varphi_3(x) = \sin \pi x_1 + x_2 + x_3$ and $\varphi_4(x) = -\sin \pi x_1 + \sin \pi x_2 + x_3$, and the initial conditions $u_0(x) = \gamma\varphi_k(x)$ with $k = 1, 2, 3, 4$ and $\gamma = 0.1$. The present numerical examples are performed using a grid with an equatorial longitude step $\Delta\lambda = \pi/96$ and a latitude step $\Delta\phi = \pi/96$, and a time step $\Delta t = 0.01$. Figures 12 and 13 show the solutions for the four cases at time $t = 5$ using Euler scheme for temporal integration. The solutions remain nearly unchanged in time for all the numerical examples considered. The L^1-error is computed by summation over the grid cells on the entire sphere. Table 2 presents the L^1-errors and the full range $u_{max} - u_{min}$ of the solutions for the four numerical tests at time $t = 5$. For all numerical examples, the L^1-error is negligible compared to the full range

Table 2: Accuracy test of the scheme using general forms of nonlinear foliated fluxes.

Function φ	L^1-error	$u_{max} - u_{min}$
φ_1	$1.18\,e-04$	0.29
φ_2	$5.30\,e-05$	0.24
φ_3	$5.60\,e-04$	0.45
φ_4	$1.25\,e-03$	0.55

of the solution $u_{max} - u_{min}$. The results clearly demonstrated the ability of the scheme to capture accurately non-trivial steady state solutions with more complex geometric forms.

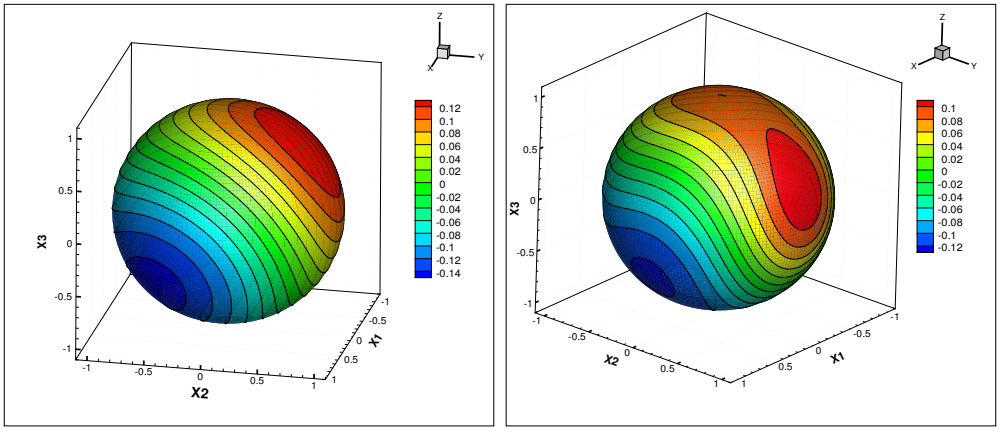

Figure 12: The numerical solution of Equation (2.10), using the nonlinear foliated flux based on the potential function $h(x, u) = \varphi(x)f(u)$ and the initial condition $u_0(x) = \gamma\varphi(x)$, at time $t = 5$ with $\gamma = 0.1$, $\Delta\lambda = \pi/96$, $\Delta\phi = \pi/96$ and $\Delta t = 0.01$. Left : solution using $\varphi_1(x) = -x_1^2 + x_2 + x_3$. Right : solution using $\varphi_2(x) = -x_1^2 + x_2^3 + x_3$.

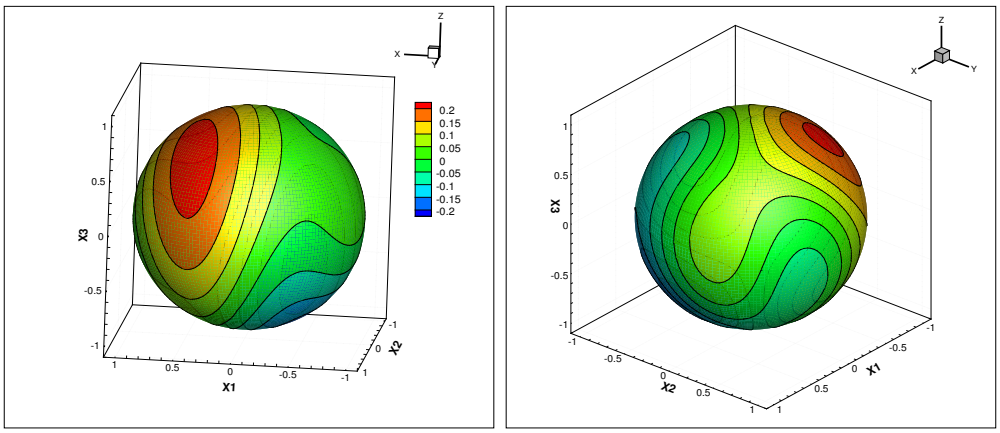

Figure 13: The numerical solution of Equation (2.10), using the nonlinear foliated flux based on the potential function $h(x,u) = \varphi(x)f(u)$ and the initial condition $u_0(x) = \gamma\varphi(x)$, at time $t = 5$ with $\gamma = 0.1$, $\Delta\lambda = \pi/96$, $\Delta\phi = \pi/96$ and $\Delta t = 0.01$. Left : solution using $\varphi_3(x) = \sin\pi x_1 + x_2 + x_3$. Right : solution using $\varphi_4(x) = -\sin\pi x_1 + \sin\pi x_2 + x_3$.

6.5. Fourth test case using generic fluxes

In this section, we consider fluxes which are not foliated. First, we consider the flux defined using the following potential function:

$$h(x,u) = x_3^3u^2 + x_3x_1u^6 \tag{6.15}$$

The numerical test is performed using the following steady state solution as initial condition:

$$u(0,x) = \begin{cases} 1, & x_3 \geq 0 \\ -1, & \text{otherwise} \end{cases} \tag{6.16}$$

We used a grid with an equatorial longitude step $\Delta\lambda = \pi/96$ and a latitude step $\Delta\phi = \pi/96$, and a time step $\Delta t = 0.01$. Figure 14 (left) shows the solution which remains unchanged at time $t = 5$ over the entire sphere. This numerical test confirms that the numerical solution is in good agreement with the analytical steady-state solution (6.16) for the generic flux based on the potential function (6.15).

In the second numerical test, we consider the generic flux defined using the following potential function:

$$h(x,u) = \theta u^2 + x_1\theta^2u^4, \tag{6.17}$$

where $\theta = x_1 + x_3\cos(\pi x_2) - \sin(\pi x_3)$.

For this flux vector field, we consider the following initial condition

$$u(0,x) = \begin{cases} 1, & \theta \leq 0 \\ -1, & \text{otherwise} \end{cases} \tag{6.18}$$

This function is a steady state solution of the system (2.10) using the flux vector field based on the potential function (6.17). This solution has a more complex form along the discontinuity curve.

The numerical test is performed using a grid with an equatorial longitude step $\Delta\lambda = \pi/96$ and a latitude step $\Delta\phi = \pi/96$, and a time step $\Delta t = 0.01$. The numerical solution at time $t = 5$ is shown in Figure 14 (right). The numerical solution is in good agreement with the analytical steady-state solution (6.18) for the generic flux based on the potential function (6.17).

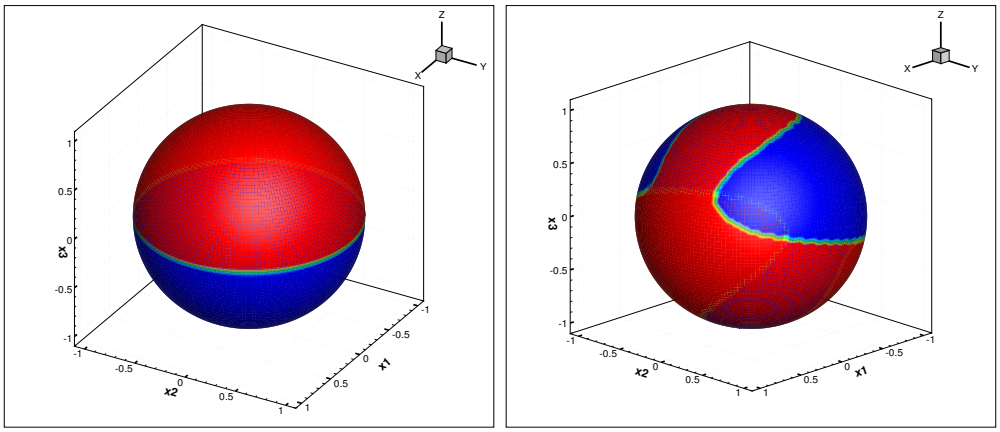

Figure 14: Left: The numerical solution at time $t = 5$ of Equation (2.10), using the generic flux based on the potential function (6.15) and the initial condition (6.16). Right: The numerical solution at time $t = 5$ of Equation (2.10), using the generic flux based on the potential function (6.17) and the initial condition (6.18).

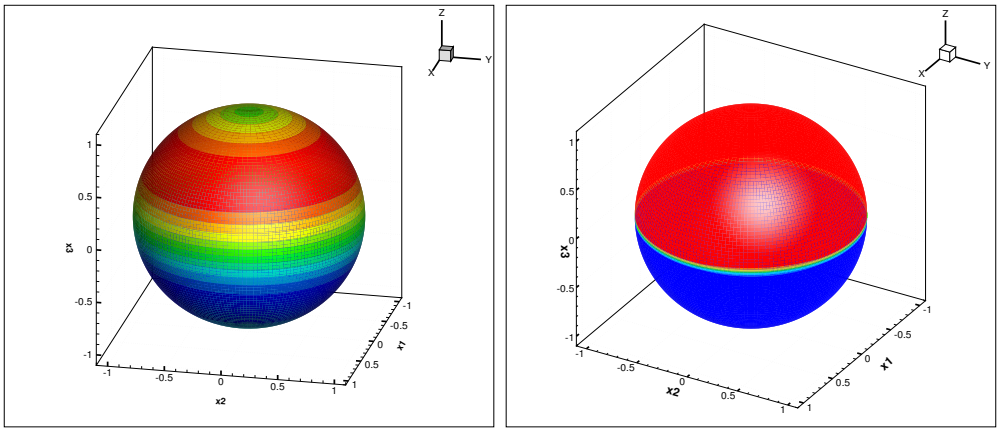

Figure 15: Left: Initial condition (6.19). Right: The numerical solution at time $t = 50000$ with $\Delta t = 0.01$, $\Delta\lambda = \pi/96$ and $\Delta\phi = \pi/96$.

The third numerical test is performed using the generic flux based on the potential function (6.15) and the following initial condition:

$$u(x, 0) = \frac{\sin(\pi x_3)}{\sqrt{1 - x_3^2}} \tag{6.19}$$

The two-dimensional view of the initial condition (6.19) and the corresponding solution for a long simulation time are shown in Figure 15. As was mentioned in the conjecture (3.4) for generic fluxes, the solution converges to a stationary solution which is constant on independent parts on the sphere. For the present numerical test, we obtain two independent domains on the sphere. The circle on the sphere defined by $x_3 = 0$ splits the sphere in two independent domains. The numerical solution presents large variations because of the generic behavior of the flux and it asymptotically tends to constant values in two independent domains. For large simulation time, the solution converges to the constant values 0.6366 and -0.6366, respectively in the domain on the sphere defined by $x_3 \geq 0$ and $x_3 < 0$ which is in good agreement with the analytical average values $2/\pi$ and $-2/\pi$ of the conservation law (2.10).

In the following, we consider a generic flux defined on the basis of the parameterized scalar potential which is composed on two different terms in order to ensure the generic behavior.

$$\begin{aligned} h(x,u) &= h_1(x)f_1(u) + h_2(x)f_2(u), \\ h_1(x) &= x_1, \qquad h_2(x) = x_2, \\ f_1(u) &= su^2/2, \;\; f_2(u) = \mu u^3/3, \quad s+\mu = 1. \end{aligned} \tag{6.20}$$

Setting the value of the parameter s allows us to observe several characters of solutions and to study the impact of each part of the scalar potential on the late-time asymptotic behaviors of solutions. First we consider the initial condition u_2 used in Test 2-b and defined by Equation (6.7). Test 2-b corresponds to the particular case $s = 1$, where the solution evolves to two constant values in two independent domains. If the parameter $s = 0.95$ is used with the same initial condition u_2, both terms of the potential function have an impact on the solution which converges to one constant value in the entire sphere. Figure 16 shows the convergence curves related to the evolution of the parameter $\|u_2(t) - \overline{u}_2\|_{L^1}$ for different values of the parameter s. For all values considered for the parameter s, the solution converges to one constant value in the entire sphere as shown in Figure 16. The evolution of the solutions and their asymptotic convergence are highly influenced by the magnitude of the different components of the potential function and the initial condition.

The entropy stability property (2.5) is now verified for the generic flux corresponding to $s = 0.5$. Figure 16, on the right, shows the evolution of the parameter $\|u_2(t)\|_{L^p_\omega(M)}$ for $p = 1, 2, 3, 4, 5, 10$ and $p = \infty$. The solution u_2 satisfies the entropy stability property for all L^p norms considered. For the generic flux with $s = 0.5$, the time-variation diminishing property (2.8) is verified for the second-order scheme using the five initial conditions u_0, u_1, u_2, u_3 and u_4, defined previously in the second test. Figure 17, on the left, presents the evolution of the parameter $\|\partial_t u\|_{\mathcal{M}}(t)$ and confirms that this parameter decreases with time, which shows that the time-variation diminishing property holds for those functions. The five pairs of functions defined in Appendix I-1 are used to check the contraction property (2.7) for the first-order scheme using the generic flux with $s = 0.5$. Figure 17 shows that the ratio parameter $E(v, w)$ is decreasing for the five pairs of functions which confirms that the contraction property holds for these pairs of functions.

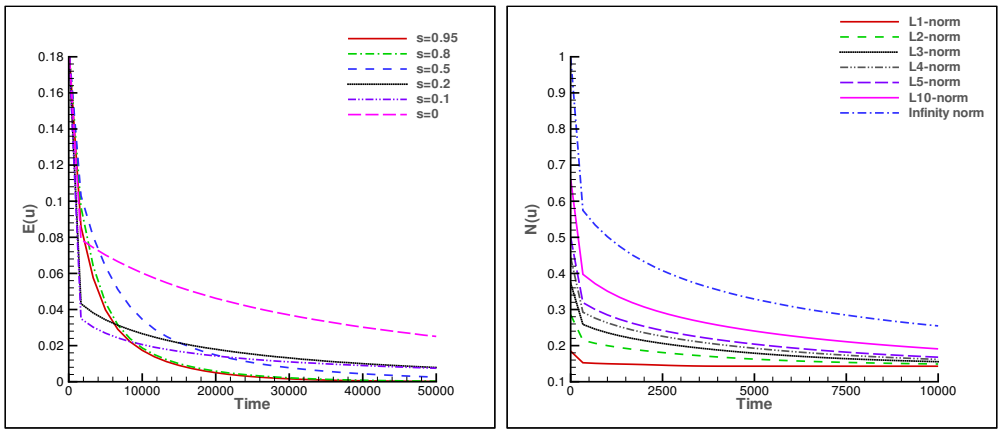

Figure 16: Convergence and stability for Test 4 with $\Delta\lambda = \pi/96$ and $\Delta\phi = \pi/96$. Left: Evolution of the parameter $E(u) = \|u_2(t) - \overline{u}_2\|_{L^1}$ for generic flux with different values of the parameter s with $\Delta t = 0.05$. Right: Entropy stability property (2.5) for the generic flux with $\Delta t = 0.01$.

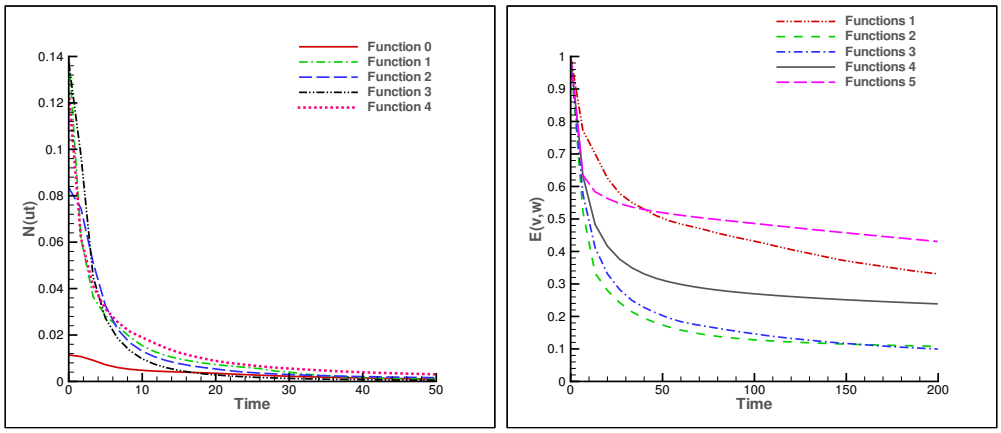

Figure 17: Time-variation diminishing property (2.8) (left) and contraction property (2.7) for the first-order scheme (right) for the generic flux with $\Delta t = 0.01$, $\Delta\lambda = \pi/96$ and $\Delta\phi = \pi/96$.

6.6. Fifth test case: revisiting the asymptotic convergence property

The aim of this section is to complete the analysis of the behavior of the solutions of Equation (2.10) for a nonlinear foliated flux. A numerical example is performed in order to cover all cases of asymptotic convergence of the solutions for nonlinear foliated fluxes. In the cases already seen in Test 2 and Test 3 for the asymptotic convergence of the solutions for nonlinear foliated flux, we observe numerically that the solution converges to constant values on independent domains on the sphere. This is a particular case of what is generally observed if the numerical scheme is more accurate and capable of simulating the solutions for a large simulation time. Then, in order to cover the other behaviors, we give more attention to the accuracy of the used scheme. To achieve this goal we consider the same second-order geometry-compatible finite volume scheme by considering a computational grid in which the sides are a part of the level sets and their equipotential curves. We consider the nonlinear foliated flux defined on the basis of the scalar potential function $h(x, u) = -x_3u^2/2$. For this

flux the level sets are the curves defined by $\phi = \phi_c$, where ϕ_c is a real constant in $[-\pi/2, \pi/2]$. The obtained level sets coincide with the sides of computational cells which ensures a very good accuracy of the scheme. The following initial condition $u_1(0, x)$ is considered:

$$u_1(0,x) = \begin{cases} x_2 + \sinh(x_1)\cos\lambda, & 0 \le \lambda \le \pi/2, \\ -x_2, & \pi/2 < \lambda < \pi, \\ x_2 + \cosh(x_3)\sin\lambda, & \text{otherwise.} \end{cases} \tag{6.21}$$

The two-dimensional view of the initial condition and the corresponding solution for a long simulation time are shown in Figure 18. The solution converges to a non-trivial stationary solution which is constant on each level set. Each constant convergence value is the average value on the corresponding level set of the function taken as an initial condition.

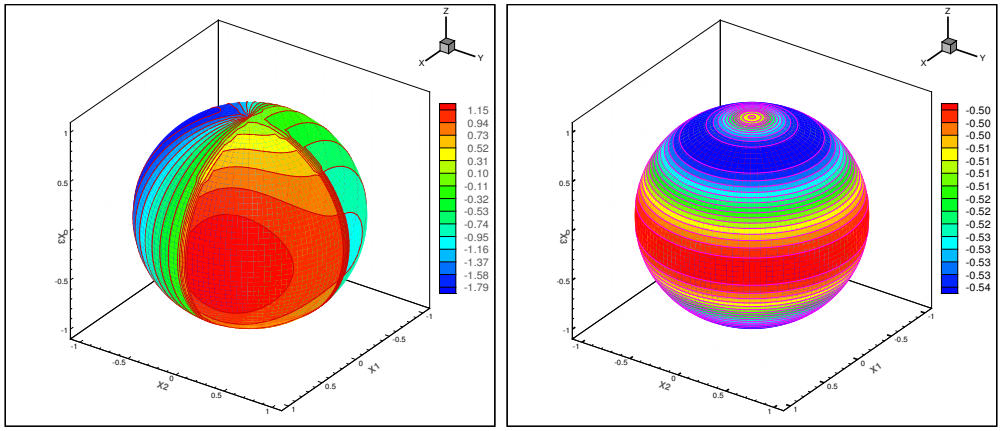

Figure 18: Initial condition u_2 (left) and solution u_2 at time $t = 50000$ (right) with $\Delta t = 0.05$, $\Delta\lambda = \pi/96$ and $\Delta\phi = \pi/96$.

6.7. Sixth test case:Williamson test case using the advection of Cosine Bell

In this section, we consider the solid-body rotation test proposed by Williamson et al. (1992). In this numerical test, the shallow water system is reduced to the scalar conservation law (2.10), where we consider the scalar level function $u(\lambda, \phi) := h(\lambda, \phi)$. This system is subject to wind forces and the flux vector due to the advecting wind is linear in u and defined as follows

$$\begin{aligned} F_\lambda(\lambda, \phi, u) &= \mathrm{U}_0 u(\cos\phi\cos\alpha + \sin\phi\cos\lambda\sin\alpha), \\ F_\phi(\lambda, \phi, u) &= -\mathrm{U}_0 u\sin\lambda\sin\alpha, \end{aligned} \tag{6.22}$$

where for the unity sphere, the magnitude of the velocity is given by $\mathrm{U}_0 = 2\pi/T$, T is the time required for the solid-body to complete one revolution around the sphere. The parameter α should be set to define the direction of the wind vector field.

This type of numerical example is used in [6] to test the GRP numerical scheme which leads to accurate results. In our case, the numerical test will be used to demonstrate the advantage of the proposed minmod reconstruction based on the values of the solution at the center of the computational cells and the values of the Riemann solutions at the cell interfaces, using the second-order approximations based on a generalized Riemann solver.

In this numerical example, we consider the following function as initial condition

$$h(\lambda,\phi) = \begin{cases} (h_0/2)(1+\cos(\pi r/R_0)), & r < R_0, \\ 0, \quad \text{otherwise}, \end{cases} \tag{6.23}$$

where for the unity sphere $R_0 = 1/3$, the height of the bell is $h_0 = 1$, and the parameter r is defined by:

$$r = arcos(\sin\phi_c \sin\phi + \cos\phi_c \cos\phi \cos(\lambda - \lambda_c)) \tag{6.24}$$

In the numerical tests, we consider the values $\lambda_c = 0$ and $\phi_c = 0$ for the coordinate of the center of the cosine bell and $T = 12$. For the orientation of the flow, we consider a deviation of $\pi/12$ from the equator.

First, the numerical test is performed using the GRP numerical scheme for two cases of minmod reconstructions. In the first case, we use the GRP scheme and the proposed minmod reconstruction based on the values of the solution at the center of the computational cells and the values of the Riemann solutions at the cell interfaces. For the second case, we consider the same minmod reconstruction without using the values of the Riemann solutions at the cell interfaces. The ratios $\tau = \|\delta u_1\|_{L^1} / \|\delta u_2\|_{L^1}$ of the mesh-size weighted L^1-norm of the error of the solutions u_1 and u_2 respectively for the two cases are computed using the time step $\Delta t = 0.01$. A numerical test is performed using a grid with an equatorial longitude step $\lambda = \pi/100$ and a latitude $\phi = \pi/100$. For this case we obtain the value $\tau = 0.6839$ at time $t = 12$. For the computational grid using $\lambda = \pi/84$ and $\phi = \pi/84$, we obtain $\tau = 0.6823$ at time $t = 12$ with $\Delta t = 0.01$. These numerical tests demonstrate that the Generalized Riemann numerical scheme performs very well when used with the proposed minmod reconstruction. Finally, a numerical example is performed using a computational grid with $\lambda = \pi/136$ and $\phi = \pi/136$ and a time step $\Delta t = 0.005$. Figure 19 (right) shows the solution after one revolution around the sphere which is in a good agreement with the initial condition shown in the same figure.

7. Concluding remarks

In this paper, numerical analyses are performed for discontinuous solutions of a class of nonlinear hyperbolic conservation laws posed on the sphere. We propose a geometry-compatible finite volume scheme using a new piecewise linear reconstruction based on the values of the solution at the center of the cells and the values of the Riemann solutions at the the cell-interfaces. These values are obtained using the second-order approximations based on a generalized Riemann solver. A total variation diminishing Runge-Kutta method with an operator splitting approach are used for time integration. With the proposed piecewise

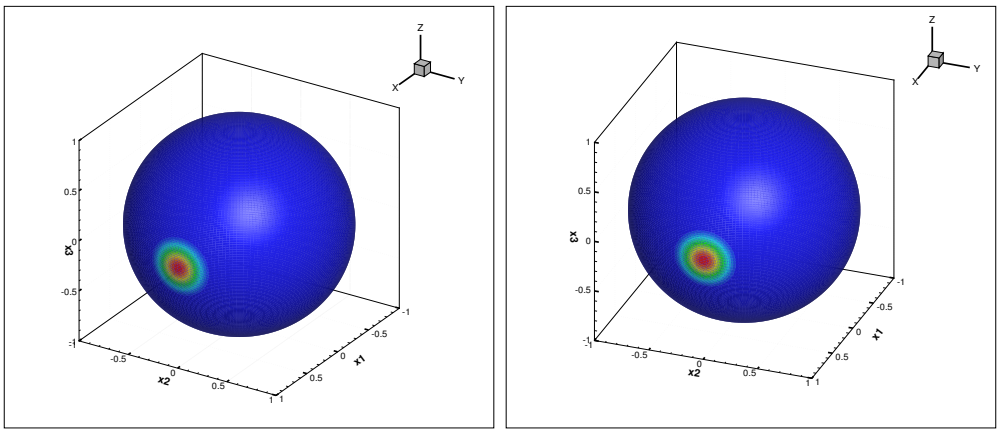

Figure 19: The cosine-bell advection test. Left : Initial condition (6.23). Right: The solution at time $t = 12$ with $\Delta t = 0.005$, $\Delta\lambda = \pi/136$ and $\Delta\phi = \pi/136$.

linear reconstruction, the numerical solutions are largely improved and the method performs well in terms of stability and accuracy for discontinuous solutions with large amplitude and shocks compared to some well-known schemes. The numerical analysis shows the second order accuracy of the scheme and that the employed splitting approach has a less impact on the third order of the accuracy of the TVD Runge-Kutta method used for temporal integration.

The first- and second-order versions of the proposed geometry-compatible finite volume scheme were investigated, and we numerically established several important properties enjoyed by discontinuous solutions defined on a curved geometry, including the contraction, time-variation monotonicity, and the entropy monotonicity properties. Furthermore, we carefully investigated the late-time asymptotic behavior of solutions, by distinguishing various types of flux potential. The following main conclusions were established for the class of nonlinear hyperbolic conservation laws and the finite volume schemes under consideration:

- The entropy stability property is valid in all L^p norms with $p \in [1, +\infty)$, and the time-variation diminishing property is satisfied by the first- and second-order schemes.

- The contraction property is satisfied by the first-order scheme but, as might be have been expected, this property is not valid for the second-order method.

- Two classes of flux were distinguished according to the structure of the flux potential. We introduced the notions of foliated flux and generic flux. The late-time asymptotic behavior of solutions was found to strongly depend on the flux (foliated or generic) as well as its (linearity or) nonlinearity. Specifically, when the flux is foliated and linear, the solutions are transported in time within the level sets of the potential. When the flux is foliated and is genuinely nonlinear, the solutions converge to their (constant) average within each level set.

- For generic flux, the solutions evolve with large variations which depend on the geometry and converge to constant values within certain "independent" domains defined on

the sphere. The number of constant values depends on curves that "split" the sphere into possibly several independent domains.

We end with a main conclusion concerning the performance of numerical schemes for foliated flux, for which the level sets play an essential role in understanding the evolution of solutions; this is especially true for genuinely nonlinear foliated flux. For such flux, we strongly recommend the use of a suitable computational mesh whenever possible in terms of implementation, not only in terms of space constraints and the desired accuracy which are commonly used for the choice of the mesh but also according to the flux vector field. More precisely, we recommend the use of a subset of the level sets of the nonlinear foliated flux as the construction lines of the computational cells. When this adjustment is respected, the steady state solutions for the nonlinear foliated flux can be captured with more accuracy and better results can be obtained for general solutions.

The extension of the techniques used in this study for the scalar conservation laws posed on the sphere to multidimensional systems and shallow water systems is not straightforward. Other techniques should be used to solve the multidimensional Generalized Riemann problem. This will the subject of our next study [4], where the concept of geometric compatibility condition that we used for the scalar conservation law will be replaced by the C-property relative to stationary solutions for shallow water system which was introduced by Vázquez-Cendón (1999). The numerical scheme that respect this property is well-balanced and it perfectly preserves the "lake at rest" steady-state solutions. We expect the extension of the techniques used in this study to shallow water systems, leads to numerical scheme for SWEs on the sphere which has the following advantages

(i) A strong link will be obtained between the numerical scheme and the governing SWEs. The C-property will be considered in analytical way in order to obtain a discrete form of the scheme that respects exactly "lake at rest" condition. A suitable discretization technique should be developed by properly taking into account the effects induced by the geometry of the two-dimensional surface of the sphere.

(ii) The quality of the solutions with large amplitude and shocks will be improved by using the resolution of the GRP and the minmod reconstruction based on the generalized Riemann values of the solutions at the interfaces and the values at the center of the cells.

8. Appendix I

In this appendix we present the pairs of functions used in Section 6 in order to analyze the contraction property (1.5) for the first-order scheme

I-1: Pairs of functions used in the second test case to check the contraction property (1.5)

$$v_1(0,x) = \begin{cases} x_2\sinh(x_1) - x_3\cosh(x_1), & x_1 \le 0, \\ x_3 + x_1, & \text{otherwise}, \end{cases}$$
$$w_1(0,x) = \begin{cases} x_2x_1^3 + e^{x_1}, & x_1 \le 0, \\ -\cos x_1 + x_3^2x_1, & \text{otherwise}, \end{cases} \tag{8.1}$$

$$v_2(0,x) = \begin{cases} x_2\cos x_1, & x_1 \le 0, \\ -x_2, & \text{otherwise}, \end{cases}$$
$$w_2(0,x) = \begin{cases} x_3\cos x_1, & x_1 \le 0, \\ -x_3 + x_3x_1\log(x_1), & \text{otherwise}, \end{cases} \tag{8.2}$$

$$v_3(0,x) = \begin{cases} x_3^2\cos(\pi x_1) + x_2, & x_1 \le 1/2, \\ -x_2 + x_3(2x_1^2 - x_1), & \text{otherwise}, \end{cases}$$
$$w_3(0,x) = \begin{cases} x_2x_3\cos(\pi x_1) + x_3(x_1^4 - x_1), & x_1 \le 1, \\ x_2x_3, & \text{otherwise}, \end{cases} \tag{8.3}$$

$$v_4(0,x) = \begin{cases} x_2e^{x_1+x_3}, & x_1 \le 0, \\ -x_2e^{x_3}, & \text{otherwise}, \end{cases}$$
$$w_4(0,x) = \begin{cases} \frac{x_2x_3}{1-x_1}, & x_1 \le 0, \\ x_1^2 - x_2x_3, & \text{otherwise}, \end{cases} \tag{8.4}$$

$$v_5(0,x) = \begin{cases} \cosh(x_1 + x_2), & x_1 \le 0, \\ -\cosh(x_2), & \text{otherwise}, \end{cases}$$
$$w_5(0,x) = \begin{cases} \cosh(x_3), & x_1 \le 0, \\ -\cosh(x_3), & \text{otherwise}. \end{cases} \tag{8.5}$$

I-2: Pairs of functions used in the third test case to check the contraction property (1.5)

$$v_1(0,x) = \begin{cases} x_2\theta + \cosh(\theta), & -\sqrt{3} \le \theta \le 0, \\ x_2\theta - \cosh(\theta), & \text{otherwise}, \end{cases}$$
$$w_1(0,x) = \begin{cases} x_2, & -\sqrt{3} \le \theta \le 0, \\ -x_2, & \text{otherwise}, \end{cases} \tag{8.6}$$

$$v_2(0,x) = \begin{cases} 1, & 0 \le \lambda \le \pi, \\ \cos\lambda, & \text{otherwise}, \end{cases}$$
$$w_2(0,x) = \begin{cases} \arcsin(x_2), & 0 \le \lambda \le \pi, \\ \cos\lambda\arcsin(x_2), & \text{otherwise}, \end{cases} \tag{8.7}$$

$$
\begin{aligned}
v_3(0,x) &= \begin{cases} e^{\theta} x_1 x_2 x_3, & -\sqrt{3} \le \theta \le 0, \\ -x_1 x_2 x_3, & \text{otherwise}, \end{cases} \\
w_3(0,x) &= \begin{cases} x_2 x_3, & -\sqrt{3} \le \theta \le 0, \\ -x_2 x_3 + e^{-1/\theta}, & \text{otherwise}, \end{cases}
\end{aligned} \tag{8.8}
$$

$$
\begin{aligned}
v_4(0,x) &= \begin{cases} \frac{\theta^2+1}{2-\theta}, & -\sqrt{3} \le \theta \le 0, \\ x_2\theta - 1/2, & \text{otherwise}, \end{cases} \\
w_4(0,x) &= \begin{cases} \frac{e^{\theta}}{\theta-1}, & -\sqrt{3} \le \theta \le 0, \\ \frac{\cosh(\theta)}{1+\theta} + x_3\theta, & \text{otherwise}, \end{cases}
\end{aligned} \tag{8.9}
$$

$$
\begin{aligned}
v_5(0,x) &= \begin{cases} \theta, & \theta \le 1, \\ \frac{x_1 \log(\theta)}{\theta} - \theta, & \text{otherwise}, \end{cases} \\
w_5(0,x) &= \begin{cases} \theta - 2\theta^3, & \theta \le 1, \\ \frac{1}{\theta} + x_2 \log(\theta), & \text{otherwise}. \end{cases}
\end{aligned} \tag{8.10}
$$

References

[1] P. Amorim, M. Ben-Artzi, and P.G. LeFloch, Hyperbolic conservation laws on manifolds: Total variation estimates and finite volume method, Meth. Appl. Analysis 12 (2005), 291–324.

[2] P. Amorim, P.G. LeFloch, and B. Okutmustur, Finite volume schemes on Lorentzian manifolds, Comm. Math. Sc. 6 (2008), 1059–1086.

[3] D. Bale, R.J. LeVeque, S. Mitran and J.A. Rossmanith, A wave-propagation method for conservation laws and balance laws with spatially varying flux functions. SIAM J. Sci. Comput. 24 (2002), 955–978.

[4] A.Beljadid and P.G. LeFloch, A well-balanced finite volume method for the shallow water system on the sphere based on a generalized Riemann solver, in preparation.

[5] M. Ben-Artzi and J. Falcovitz, *Generalized Riemann problems in computational fluid dynamics*, Cambridge University Press, London, 2003.

[6] M. Ben-Artzi, J. Falcovitz, and P.G. LeFloch, Hyperbolic conservation laws on the sphere. A geometry-compatible finite volume scheme, J. Comput. Phys. 228 (2009), 5650–5668.

[7] M. Ben-Artzi and P.G. LeFloch, The well posedness theory for geometry compatible hyperbolic conservation laws on manifolds, Ann. Inst. H. Poincaré Anal. Non Linéaire 24 (2007), 989–1008.

[8] J.L. Bona, V.A. Dougalis, O.A. Karakashian, W.R. McKinney, Conservative, high-order numerical schemes for the generalized Korteweg-de Vries equation, Phil. Trans. Roy. Soc. London Ser. A 351 (1995), 107–164.

[9] M.J. Berger, D.A. Calhoun, C. Helzel, and R.J. LeVeque, Logically rectangular finite volume methods with adaptive refinement on the sphere, Philos. Trans. R. Soc. Lond. Ser. A 367 (2009), 4483–4496.

[10] A. Bourgeade, P.G. LeFloch, and P.-A. Raviart, An asymptotic expansion for the solution of the generalized Riemann problem. Part II. Application to the gas dynamics equations, Ann. Inst. H. Poincaré, Nonlin. Anal. 6 (1989), 437-480.

[11] D.A. Calhoun, C. Helzel and R.J. LeVeque, Logically rectangular finite volume grids and methods for 'circular' and 'spherical' domains. SIAM Rev. 50 (2008), 723–752.
[12] G. Dziuk and C. M. Elliott, Finite elements on evolving surfaces, IMA J. Numer. Anal. 27:262–292, 2007.
[13] D. Dziuk, D. Kroöner, and T. Müller, Scalar conservation laws on moving hypersurfaces, Interf. Free Bound., to appear.
[14] FX Giraldo, Lagrange-Galerkin methods on spherical geodesic grids: the shallow water equations. Journal of Computational Physics 160 (2000), 336–368.
[15] J. Giesselmann, A convergence result for finite volume schemes on Riemannian manifolds,
[16] F.X. Giraldo, High-order triangle-based discontinuous Galerkin methods for hyperbolic equations on a rotating sphere, Journal of Computational Physics 214 (2006), 447–465.
[17] F.X. Giraldo, A spectral element shallow water model on spherical geodesic grids, International Journal for Numerical Methods in Fluids 35 (2001), 869–901.
[18] F.X. Giraldo, J.S. Hesthaven, T. Warburton, Nodal high-order discontinuous Galerkin methods for the spherical shallow water equations, Journal of Computational Physics 181 (2002), 499–525.
[19] F.X. Giraldo, T. Warburton, A nodal triangle-based spectral element method for the shallow water equations on the sphere, Journal of Computational Physics 207 (2005), 129–150.
[20] G.J. Haltiner, *Numerical weather prediction*, John Wiley Press, 1971.
[21] K. K. Katta, R. D. Nair, and V. Kumar, High-Order Finite-Volume Transport on the Cubed Sphere: Comparison between 1D and 2D Reconstruction Schemes, Monthly Weather Review 143 (2015), 2937-2954.
[22] S.N. Kruzkov, First-order quasilinear eequations in several independent variables, Math. USSR Sb. 10 (1970), 217–242.
[23] A. Kurganov and G. Petrova, Central-ipwind schemes on triangular grids for hyperbolic systems of conservation laws, Numerical Methods for Partial Differential Equations, 21, 536-552 (2005)
[24] J.O. Langseth and R.J. LeVeque, A wave-propagation method for three-dimensional hyperbolic conservation laws, J. Comput. Phys. 165 (2000), 126–166.
[25] P.G. LeFloch, Hyperbolic conservation laws on spacetimes, in "Nonlinear conservation laws and applications", IMA Vol. Math. Appl. 153, Springer, New York, 2011, pp. 379–391.
[26] P.G. LeFloch and H. Makhlof, A geometry-preserving finite volume method for compressible fluids on Schwarzschild spacetime, Commun. Comput. Phys. 15 (2014), 827–852.
[27] P.G. LeFloch, H. Makhlof, and B. Okutmustur, Relativistic Burgers equations on curved spacetimes. Derivation and finite volume approximation, SIAM J. Numer. Anal. 50 (2012), 2136–2158.
[28] P.G. LeFloch and B. Okutmustur, Hyperbolic conservation laws on spacetimes. A finite volume scheme based on differential forms, Far East J. Math. Sci. 31 (2008), 49–83.
[29] P.G. LeFloch and P.-A. Raviart, An asymptotic expansion for the solution of the generalized Riemann problem. Part I. General theory, Ann. Inst. H. Poincaré, Nonlinear Analysis 5 (1988), 179–207.
[30] R.J. LeVeque, Balancing source terms and flux gradients in high-resolution Godunov methods: The quasi-steady wave-propagation algorithm, J. Comput. Phys (1998), 346–365.
[31] R.J. LeVeque, *Finite volume methods for hyperbolic problems,* Cambridge University Press,

Cambridge, 2002.

[32] C. Ronchi, R. Acono, and P.S. Paolucci, The cubed sphere: a new method for the solution of partial differential equations in spherical geometry, J. Comput. Phys. 124 (1996), 93–114.

[33] A. Rossmanith, D.S. Bale, and R.J. LeVeque, A wave propagation algorithm for hyperbolic systems on curved manifolds, J. Comput. Phys. 199 (2004), 631–662.

[34] A. Rossmanith, A wave propagation method for hyperbolic systems on the sphere, J. Comput. Phys. 213 (2006), 629–658.

[35] V. V. Rusanov, Calculation of interaction of non-steady shock waves with obstacles, J. Comput. Math. Phys. USSR, 1 , 267-279, 1961.

[36] G. Russo, Central schemes for conservation laws with application to shallow water equations, S. Rionero, G. Romano Ed., Trends and Applications of Mathematics to Mechanics: STAMM 2002, Springer Verlag, Italy, 2005, pp. 225–246.

[37] G. Russo, High-order shock-capturing schemes for balance laws, in "Numerical solutions of partial differential equations", Adv. Courses Math. CRM Barcelona, Birkhäuser, Basel, 2009, pp. 59–147.

[38] M.-E Vázquez-Cendón, Improved treatment of source terms in upwind schemes for the shallow water equations in channels with irregular geometry. Journal of Computational Physics, 148, 497-526, 1999

[39] D. L. Williamson, J. B. Drake, J. J. Hack, R. Jakob, and P. N. Swarztrauber, A standard test set for numerical approximations to the shallow water equations in spherical geometry, J. Comput. Phys., 102:211–224, 1992.